Generation of electronically unsaturated carbon sites on carbon materials and study of their magnetic and chemical properties

Mathieu Vidal, Maryam Dehaghani, Javier Navarro-Ruiz, Takeharu Yoshii, Keigo Wakabayashi, Hirotomo Nishihara, Mathias Barreau, Fabrice Bournel, Jérôme Volkman, Guillaume Clet, et al.

Generation of Electronically Unsaturated Carbon Sites on Carbon Materials and Study of their Magnetic and Chemical Properties

Mathieu Vidal,[a] Maryam S. Dehaghani,[b] Javier Navarro-Ruiz,[b] Takeharu Yoshii,[c] Keigo Wakabayashi,[c] Hirotomo Nishihara,[c] Mathias Barreau,[d] Fabrice Bournel,[e,f] Jérôme Volkman,[a] Guillaume Clet,[g] Spirydon Zafeiratos,[d] Nolwenn Le Breton,[h] Pascal Puech,[i] Iann C. Gerber,[b] Athanassios K. Boudalis,[h] Thomas Blon,[b] and Philippe Serp[a,j*]

[a] *LCC-CNRS, Université de Toulouse, UPR 8241 CNRS, UPS, INPT, 31030 Toulouse, France*

[b] *LPCNO, INSA−CNRS−UPS, Université de Toulouse, 135 Avenue de Rangueil, 31077 Toulouse, France*

[c] *Advanced Institute for Materials Research (WPI-AIMR)/Institute of Multidisciplinary Research for Advanced Materials, Tohoku University, 2-1-1 Katahira, Aoba-ku, Sendai, Miyagi 980-8577, Japan*

[d] *ICPEES-UMR 7515 CNRS-ECPM-Université de Strasbourg, 67087 Strasbourg Cedex 2, France*

[e] *Laboratoire de Chimie Physique-Matière et Rayonnement, Sorbonne Université, Campus Curie, CNRS UMR 7614, 4 place Jussieu, 75005 Paris, France*

[f] *Synchrotron SOLEIL, L'Orme des Merisiers, B.P. 48, Saint Aubin, 91192 Gif-sur-Yvette Cedex, France*

[g] *Université de Caen Normandie, ENSICAEN, CNRS, LCS, 14000 Caen, France*

[h] *Institut de Chimie de Strasbourg UMR 7177, 1 rue Blaise Pascal, BP 296 R8, 67008 Strasbourg Cedex, France*

[i] *Centre d'Élaboration de Matériaux et d'Études Structurales (CEMES), 29 rue Jeanne Marvig, 31055 Toulouse, France*

[j] *Institut Universitaire de France (IUF), 1 rue Descartes75231 Paris Cedex 05, France*

ABSTRACT: The presence of defects in carbon materials, such as electronically unsaturated carbon sites, can profoundly affect their magnetic ordering and chemical reactivity. The detailed analysis of these species (edge states, σ free radicals or carbene), which are pivotal for many applications, remains a significant challenge for carbon bulk materials. Today, the engineering of defective carbon material often relies on the use of hardly up-scalable physical methods not accessible to synthetic chemists. It is therefore important to develop simple and scalable methods to generate well-defined electronically unsaturated sites in carbon materials. Herein, we followed the transformation and evolution of surface oxygen functional groups of various oxidized carbon materials during thermal treatment under an inert atmosphere using various analytical techniques and *ab-initio* molecular dynamics, with the aim of producing stabilized localized electronic states from condensation reactions. Synchrotron-based *in situ* XPS analyses show a decrease of carboxylic surface groups with a concomitant increase of defect sites upon defunctionalization, which is expected from condensation reactions. Echo-detected field-swept EPR spectra show the apparition of a signal only upon defunctionalization, particularly for samples showing a high proportion of prismatic surface. The contribution of these electronically unsaturated carbon sites to the catalytic activity for the catalytic oxidative dehydrogenation of indoline is moderate, and the surface oxygen functional groups are the main active sites.

TOC Graphic

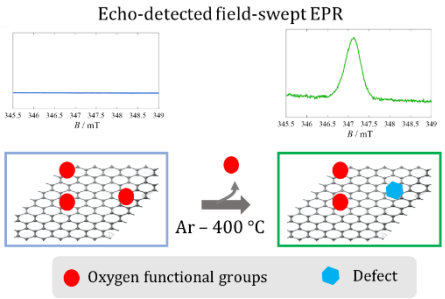

1. INTRODUCTION

"*Carbon is often described as one of the most long-established, and yet newest material to be used in technology*".[1] Although dating from 1967, E. Fitzer's statement is still relevant today, highlighting carbon's chemistry and physics richness. While the intrinsic properties of sp^2 carbon materials, such as electronic conduction or mechanical properties are sought after for some applications; for other applications, the presence of structural irregularities (defects) in the carbon network is necessary. Properties such as magnetic ordering, charge transport, light emission or chemical reactivity, which can be intercorrelated, are indeed dependent on the charge state and electronic excitation of localized sites, which are related to the presence of carbon p_z vacancies or edges in the network of defective carbon materials (*DCM*). Thus, the magnetic[2] and chemical reactivity[3] properties of carbon materials have been demonstrated to closely correlate to the presence of such defects; even if their exact nature is still the subject of debates.

Three types of localized electronic states and spins have been identified (Scheme 1). First, edge states, which appears as a nonbonding π-electron state originating from C $2p_z$ orbitals at H-terminated zigzag edge sites.[4] The electronic properties of these edge localized states are significantly affected by the level of edge hydrogenation.[5] The local chemical structure around the zigzag-shaped edge is described by the resonance of three degenerated formulas with chemically reactive radical characters at the edge sites. These localized states with corresponding energy levels at E_F are reminiscent of the radical character of the non-Kekulé type Clar structures in alternant polycyclic aromatic hydrocarbons.[6,7] On soot precursors, the localization of π-electrons on non-hexagonal aromatic rings was found to allow for a triplet diradical ground state.[8] Second, σ free radicals at carbon dangling bonds in closed spaces that ensure their survival from exposure to air. Third, carbene and aryne-type sites on non-hydrogenated edges or large vacancies.[9] Since the studies on the subject extend from physics to physical-chemistry up to organic chemistry, it is difficult to get a unified vision on the subject.[10] It seems to us that the molecular vision of the problem, introduced by L. Radovic in a land-mark paper, is very relevant and constitutes a good entry point.[11] On hydrogen-free armchair edges, aryne-like sites should exist, with the singlet ground state being most common. Such sites have been experimentally evidenced.[12] On hydrogen-free zig-zag edges, these sites are carbene-like and the more stable sites are in the triplet state. Density functional theory (DFT) studies of the spin coupling around a carbon single vacancy (*SV*) in graphene have shown that the triplet state is slightly more stable (4.6 kcal·mol^{-1}) than the singlet state.[13] As for edges, the ground state's stability depends on their type: *zigzag*-triplet or *armchair*-singlet.[11] Only the

structures having a triplet ground state contribute to the material's magnetic susceptibility[14] and chemical reactivity.[15] These sites are expected to have a short lifetime due to their high chemical reactivity towards oxygen, water or H_2.[16,17] However, the stability of carbon vacancies increases with their size, since the formation of pentagons eliminates the carbene sites, and that of the *zigzag*-triplet-edge sites with the size of the graphene sheet, as a result of resonance stabilization. Furthermore, it has been proposed that some of these sites at the zigzag edge or in basal plane vacancies could survive oxygen, water or H_2 exposure, stabilized with respect to conventional free radicals by virtue of π-electron localization and consequent formation of π-σ pairs.[10] In addition, DFT calculations have suggested that the introduction of surface oxygen functional groups (OFGs) near large vacancy sites, plays an important role in stabilizing unpaired spins.[18] It was also proposed that isolated paramagnetic centers can also exist as unfunctionalized carbon atoms in the basal planes present in highly functionalized regions rich in OFGs.[19] Finally, in graphite oxide the majority of paramagnetic centers were proposed to be oxygen-centered radicals; the structure of which consisting in hydroxyl or carboxyl groups in the vicinity of oxygen-centered radicals of phenol and semiquinone types.[20] Consequently, on the real large vacancies or edge planes of *DCM*, there must be hydrogen atoms (edge states), OFGs and possibly some stabilized triplet carbene sites if they survive air/H_2 exposure.

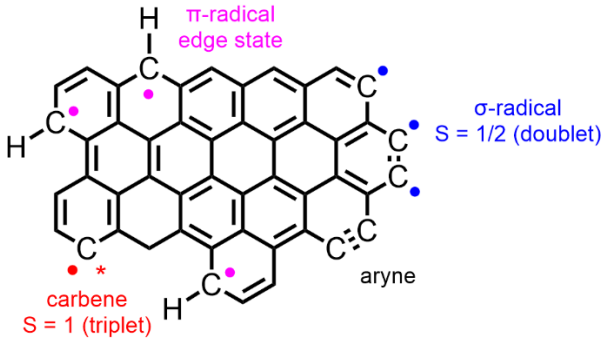

Scheme 1. Proposed types of localized electronic states and spins in large vacancies or edge planes of carbon materials.

Most of the work related to *DCM* engineering rely on the use of hardly up-scalable physical methods not accessible to synthetic chemists, such as electron or ion irradiation.[21] Alternatively, mechanochemistry (milling/grinding processes) is a commonly used method to shattering crystals or introducing defects in carbon materials.[22] However, contamination from milling vials and grinding balls is one of the major problems of this approach, which can lead to errors in the interpretation of reactivity or magnetism results due to the presence of impurities, which

may be metallic.[23] A more attractive method consists in the thermally- or microwave-assisted decomposition of oxygen or nitrogen surface functional groups, which can generate significant amount of topological defects and vacancies in the carbon lattice. Thus, it has been proposed that annealing under an inert atmosphere removes oxygen in the form of CO_2 at relatively low temperatures (< 600 °C) and CO predominantly at high temperatures (500-1100 °C), leaving unsaturated carbon atoms.[24-28] The activated surface, containing carbon sites with high chemical reactivity and short lifetime, is capable of activating H_2, readsorbing oxygen or strongly adsorbing water at room-temperature.[24,27-29] Some proposed reactions for the transformation and evolution of OFGs during thermal treatment under an inert atmosphere are shown on Scheme 2 (here carboxylic and phenol groups). Simulations by *ab-initio* molecular dynamics (*AIMD*) have shown that the reaction between a -COOH and a vicinal -OH group (Scheme 2a) is thermodynamically favorable.[30]

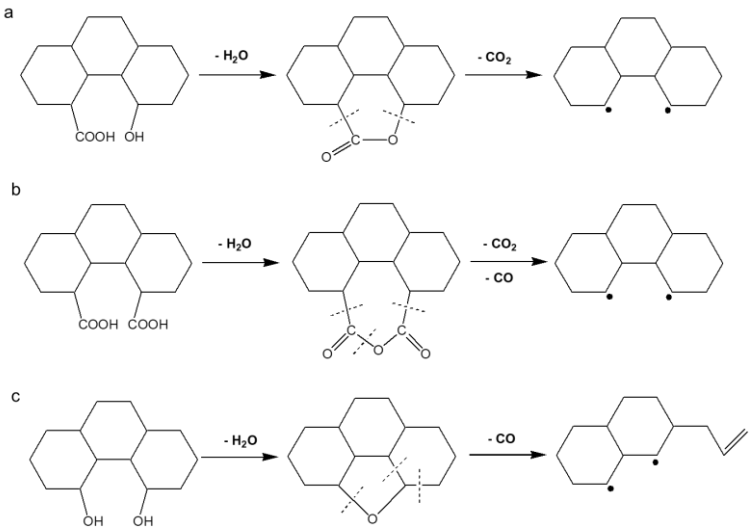

Scheme 2. Proposed pathway for transformation and evolution of OFGs during thermal treatment under inert atmosphere possibly leading to stabilized localized electronic states. Adapted from ref. [25].

As far as carboxylic group decomposition is concerned, it is worth mentioning that, in the field of polymer chemistry, decarboxylation-induced cross-linking reactions have been proposed,[31,32] which involved two vicinal carboxylic groups as in Scheme 2b. During this decarboxylation process, radical-induced cross-linking occurs via an anhydride intermediate. First, two -COOH groups in adjacent moieties form the anhydride during heating under inert gas flow. Then, the anhydride is decarboxylated by release of a CO_2 and a CO, thereby creating two phenyl free radicals that combine to form linkages yielding biphenyl cross-linking.[31] Free-radical chemistry was also evoked to rationalize the decomposition of biphenyl carboxylic

acids.[33] It is also worth mentioning that CO_2 but also CO were detected during benzoic acid thermal decomposition that occur by both molecular and radical processes. In that case, phenyl radicals are present leading to the formation of biphenyls.[34] Similarly, the most probable mechanism of terephthalic acid thermal decomposition involves the reactions of the radical intermediates that are formed at high temperatures via a free radical mechanism.[35] As far as phenolic group decomposition is concerned (Scheme 2c), the cyclic dehydration of vicinal diols to ether or epoxy (dehydrative epoxidation) is a well-known reaction of industrial interest that can be catalyzed.[36] In addition, it has been shown that the thermal degradation of oxymethylene ethers[37] or some epoxy resins[38] results in the formation of carbene and radical sites, respectively. Such gas-phase thermochemical method have already been used for the organic functionalization of various carbon materials[39-42] and for supported metal single atom stabilization.[43,44] Consequently, the engineering and study of *DCM* is of great scientific and technological importance for various fields such as information storage,[45] quantum information,[46] nanoelectronics,[47] photonics/plasmonics,[48,49] interstellar[50] and tropospheric chemistry[51], as well as catalysis.[52,53]

In this work, the effect of a heat treatment under an inert atmosphere at 400 °C, a temperature at which carboxylic groups are decomposed, on the structural, textural, chemical and magnetic properties of four graphitic carbon materials is described. A particular attention has been devoted to the evolution of the surface chemistry/reactivity and magnetic properties, which have been probed by a variety of techniques such as HT-temperature programmed desorption (TPD), X-Ray photoelectron spectrometry (XPS), molecular dynamics simulations (MDs), vibrating sample magnetometry (VSM), electron paramagnetic resonance (EPR), and catalytic activity tests.

2. MATERIALS AND METHODS

2.1. Oxidation and thermal defunctionalization of graphitic carbons. The materials were functionalized by a treatment with HNO_3 (HNO_3 69% Suprapur, Sigma Aldrich) under reflux at 140 °C for 3 h. The mixture was then filtered and washed with distilled water until neutral pH was obtained. The finals products were then dried at 80 °C overnight. The carbon materials were then activated in a horizontal tubular oven under Ar (210 mL min^{-1}) at 400 °C for 1 hour and kept under argon in a glove box for analysis. The activation was done prior each catalysis with oxidized materials to avoid any transformation or evolution of the catalysts with time.

2.2. Instrumentation. Raman spectra were obtained on a micro-Raman setup (Una LabRam HR800 Jobin Yvon spectrometer). A laser of 532 nm wavelength was used as excitation source

with a maximum power of 7 mW. For in situ Raman measurements under heating, the solids were placed in a Linkam CCR-1000 cell which was heated in a flow of 20 mL min^{-1} Ar for 3 consecutive steps at 200, 400 and 600 °C (heating: 10°C min^{-1}, *ca*. 40 min at each temperature). Raman spectra were acquired with a Horiba Labram HR Evolution equipped with a laser at 532 nm, a 600 lines mm^{-1} grating and a 50x SLWD objective.

X-ray powder diffraction patterns were obtained at room temperature with a MiniFLex600 diffractometer, employing Cu K_α radiation (λ = 1.54187 Å). Measurements were recorded from 2Θ = 10-90 ° at a scanning speed of 2 ° min^{-1}.

The ATG measurement were obtained on a METTLER TOLEDO TGA 2 apparatus. The materials were heated at 110 °C for 20 minutes (10 °C min^{-1}) then at 1000 °C for 15 minutes (10 °C min^{-1}) under air (5 mL min^{-1}).

TEM analyses were performed by using a JEOL JEM 1400 electron microscope operating at 120 kV. The high-resolution analyses were conducted by using a JEOL JEM 2100f microscope equipped with a field emission gun (FEG) operating at 200 kV with a point resolution of 2.3 Angstrom and a JEOL JEM-ARM200F Cold FEG operating at 200 kV with a point resolution of > 1.9 Å.

HT-TPD analysis was performed up to 1800 °C at a heating rate of 10 °C min^{-1} using an advanced TPD system.[54,55] CO, CO_2, H_2O, and H_2 are released during heating by the thermal decomposition of OFGs and H-terminated edge sites.

X-ray photoemission spectra were measured in three different apparatuses, employing dual, monochromatic, and synchrotron radiation X-ray sources (Table S1). This was done to ensure the reproducibility of the measurements and the consistency of the applied peak fitting procedure. The first spectrometer is equipped with a RESOLVE 120 MCD5 hemispherical electron analyzer and an achromatic Mg K_α hν = 1486.6 eV dual anode X-ray source.[56] The second consists of a VSW Class WA hemispherical electron analyzer and a monochromatic Al Ka X-ray source (1486.6 eV).[57] Finally, experiments were also carried out at the NAP-XPS end station of Sorbonne Université attached to the TEMPO beamline of the SOLEIL Synchrotron radiation facility.[58] For all instruments the electron take-off angle to the surface was of 90°. Below follows a table comparing the measurement conditions employed in each apparatus. Both survey scans and high-resolution spectra were collected for all carbon materials before and after the calcination treatments. The spectra were fitted after Shirley background subtraction, using CasaXPS v2.3.25 software.[59] The photoelectron binding energy (BE) are referred to the Fermi-level of the analyzer, and reported as measured without any correction. A Shirley background subtraction The C 1s spectra were fitted by Doniach-Sunjic functions, while

symmetric Gaussian-Laurentian profiles were used for the O 1s peaks. The amount of surface oxygen was determined from the relative areas of the C 1s and O 1s peaks, considering the dependence of the photoemission cross-sections to the X-ray radiation energy.[60] The samples were taken out of oven after the heat treatment and exposed to air prior to the introduction into the X-ray photoelectron spectroscopy (XPS) apparatus.

Nitrogen adsorption measurements were performed at -196 °C using a 3Flex Surface Characterization Analyzer (Micromeritics GmbH). Before analysis, the samples were degassed at 150 °C using a Micromeritics VacPrep 061 Sample Degas System until a static pressure of less than 0.01 Torr (0.0133 mbar) was reached.

Magnetic measurements were performed using a Quantum Design Physical Property Measurement System (PPMS) in the Vibrating Sample Magnetometer (VSM) configuration. The samples were prepared by compacting few mg of the named materials powder into a nonmagnetic elongated capsule in ambient atmosphere. 5 T magnetization cycles were recorded at 300 K and 5 K after a 5 T field cooling. Magnetic susceptibility was recorded applying 5 T between 5 K and 300 K after field cooling. The data were fitted by the Curie-Weiss law: $\chi = \chi_0 + C/(T-\theta)$ where χ_0, C, T, and θ are a temperature-independent term, the Curie constant, the temperature and the Curie-Weiss temperature, respectively.[61] N_{spin} was then determined using the deduced value for C, according to the following equation: $C = \left(N_{spin} g^2 {\mu_B}^2 S(S+1)\right)/3k_B$, where g, μ_B, S, and k_B are the g-factor, the Bohr magneton, the total spin quantum number assumed to be ½ (free spins), and the Boltzmann constant respectively.

EPR spectra were recorded on a EMX plus spectrometer (Bruker Biospin GmbH) equipped with a high sensitivity resonator (4119-HSW, Bruker). A small amount (few mg) of samples was introduced in EPR tubes (CFQ OD 4 mm, Wilmad-LabGlass) sealed under helium atmosphere. The microwave power was 1.2 mW and the modulation amplitude was 0.3 mT. Spin quantification was done by comparing the double integral of the EPR spectra to the double integral of a freshly homemade standard consisting of mixture of DPPH in KCl. Pulsed EPR spectra were recorded on an Elexsys E580 spectrometer (Bruker Biospin GmbH) equipped with a 4118-MD5X resonator and a CF935 continuous flow cryostat controlled by a Mercury ITC (Oxford Instrument). The pulses were amplified using a 1 kW travelling wave tube amplifier. The shot repetition time was set at at least 5 times T_1 and the number of shot per point was adjusted according to the signal to noise ratio. The duration of the impulsions were 16 ns and 32 ns for π/2 and π pulses respectively. Hahn echo sequence (π/2 – τ – π – τ – echo) was used

to record the echo detected field sweep (EDFS) and T_2. For T_2 measurements, the delay τ started at 290 ns and was incremented by steps of 8 or 12 ns. Picket fence saturation recovery sequence $(\pi - t -)_n\ \pi/2 - \tau - \pi - \tau -$ echo was used to measure T_1 with n equal to 28, t equal to 100 ns and τ equal to 290 ns. Nutations experiments were recorded by applying a nutation pulse p_{nut} of incremented duration followed by a Hahn echo sequence applied after a long decoherence time $t_{dec} > 5*T_M$ ($t_{nut} - t_{dec} - \pi/2 - \tau - \pi - \tau -$ echo). The length of the π/2 and π pulses were adapted to get the maximum intensity of the echo at each power. T_M and T_1 curves were fitted using a homemade Matlab (MathWorks) routine. T_M curves were fitted using a stretched mono-exponential of the following form:

$$M_z(t) = M_0 e^{-(t/T_2)^{\beta}} \qquad (1)$$

Were M_0 is the amplitude and β is the stretch factor.

T_1 curves were fitted with stretched mono-exponential of the form:

$$M_z(t) = M_0(1 - e^{-(t/T_1)^{\beta}}) \qquad (2)$$

were M_0 is the amplitude and β is the stretch factor.

2.3. Computational details. Periodic DFT simulations were performed using the *ab initio* plane-wave pseudopotential approach, as implemented in the Vienna Ab initio Simulation Package (VASP 6.4).[62,63] The Perdew-Burke-Ernzerhof exchange-correlation functional[64] within the generalized gradient approximation was chosen, and van der Waals interactions were taken into account through the D3 method of Grimme *et al.* with zero-damping function.[65] The innermost electrons were replaced by a projector-augmented wave (PAW) approach,[66,67] while the valence monoelectronic states were expanded in a plane-wave basis set with a cutoff energy of 500 eV. As previously computationally modeled and described,[68] the model carbon material consists of an oxygen-functionalized graphene including experimentally probed abundant OFGs and point defects. A Γ-centered 1×1×1 *k*-point grid generated using the Monkhorst–Pack method[69] was employed (a sufficiently large supercell is used), and iterative relaxation of atomic positions proceeded until the change in total energy was less than 10^{-6} eV. Spurious interactions between the modeled slab and its perpendicular periodic images were eliminated by introducing a vacuum region by at least 10 Å and by applying a dipole correction to the total energy along the *z*-direction.[70]

The thermal stability of the graphitic material was studied by performing first-principle Born−Oppenheimer *AIMD* simulations. Following a temperature range from 0 K to 1800 K (temperatures at which the carbons were experimentally heat-treated), the simulation system was propagated without any symmetry constraints for 9, 18, 36, and 90 ps, corresponding to

heating rates of 200, 100, 50, and 20 K ps^{-1}, respectively. The Verlet algorithm was used to solve the Newton equations of motion and the time step was set to 0.5 fs. The temperatures fluctuating around the equilibrium values were balanced using the Nosé thermostat.[71]

2.4. Catalytic experiments. Oxidation of indoline was performed in a glass balloon of 50 mL with a magnetic stirrer. In a typical experiment, the activated material (350 mg) was added in the balloon under argon and a mixture containing 20 mL of indoline solution (VWR APOSOR6520, 0.3 mmol) in xylene (Sigma Aldrich mixture of isomers) and biphenyl (Merck, 0.3 mmol, internal standard) was then added. O_2 was bubbled for 10 min at 20 mL min^{-1} then the mixture was put under reflux at 100 °C in an oil bath with an O_2 flow set at 5 mL min^{-1}. Argon flux was stopped when oxygen bubbling began. The stirring was fixed at 700 rpm. The reaction was followed for 5 hours taking a sample every hour. Samples of the reaction mixture were analyzed by GC.

3. RESULTS AND DISCUSSION

Four carbon materials, including few-layer graphene (FLG), carbon nanotubes (CNTs), carbon nanofibers (CNFs, fishbone type) and a fibrous material (FMs) presenting a disordered surface structure have been used. These materials were first submitted to a high temperature graphitization treatment at 2800 °C in order to eliminate residual metals and reduce the quantity of structural defects. The full characterization of the graphitized samples, including their basal/prismatic surface ratio was already reported,[72] and will be remembered only when needed. Basically, graphitized FLG and CNT possess a higher percentage of basal surface (≈75%) compared to CNF and FM (≈40%). Subsequently, the graphitized materials were oxidized in boiling ultrapure nitric acid (metal impurities at ppt level) to introduce OFGs, and defunctionalized at 400 °C under argon to introduce electronically unsaturated carbon sites.

3.1. Oxidized carbon materials. As traces of metallic impurities can be detrimental for the accuracy of several analyses such as HT-TPD, VSM and EPR, their presence on the oxidized samples was checked by ToF-SIMS analyses. The Figure S1a shows the evolution of iron and cobalt content (catalyst residue) in the case of CNTs for the pristine (CNT_P), graphitized (CNT_G) and graphitized and oxidized (CNT_O) samples. From these analyses, it can be concluded that the investigated materials are free of metallic impurities arising from the $AlFeCoO_4$ catalyst. The main impurity introduced during the HNO_3 treatment was sodium (Figure S1b). ToF-SIMS analyses were also used to evaluate the subsurface C/O ratio for the four oxidized materials taken into account the main fragments containing CH and CO functionalities. As can be seen in Figure S1c, the C/O ratio follows the order FLG_O > CNT_O >

CNF_O > FM_O, pointing to the introduction of a higher content of OFGs for carbon materials presenting high level of prismatic surface (the prismatic surface in these materials follows the order FLG_P < CNT_P < CNF_P < FM_P).[72]

High- and low-resolution TEM micrographs of the four oxidized materials are shown on Figure 1 and Figure S2, respectively. The FLG presents several graphene layers consistent with its low surface area (S_{BET} = 28 m^2 g^{-1}, Table 1), as well as many surface defects resulting from the oxidation. Such oxidative debris, which are frequently observed in graphene oxide[73] and are composed of sp^2 aromatic domains with OFGs located mainly on the edges, are visible in Figure S3. These debris, whose size can reach several nm,[2 74] adhere to the graphene flake surfaces *via* non-covalent interactions and are present even in samples purified by standard methods. The CNT_O (S_{BET} = 144 m^2 g^{-1}) have an external diameter of around 15 nm and present graphene layers parallel to the tube axis, as well as few internal arches (bamboo-like structure). Few oxidation debris resulting from the HNO_3 treatment are visible on their surface. The CNF_O (S_{BET} = 103 m^2 g^{-1}) with a bamboo-like structure present a bimodal diameter distribution (large CNFs of ~150 nm and smaller ones of ~30 nm, Figure S2), and their graphene layers show an angle of 10-30 ° relative to the fiber axis. The FM_O (S_{BET} = 64 m^2 g^{-1}) contains fibers of various diameters (20-200 nm) with a non-hollow structure. Most edges of CNF_O and FM_O are open and few closed loops are visible (Figure S4). Oxidation debris are also observable on these two samples, although in lower quantities compared to CNT_O and particularly FLG_O.

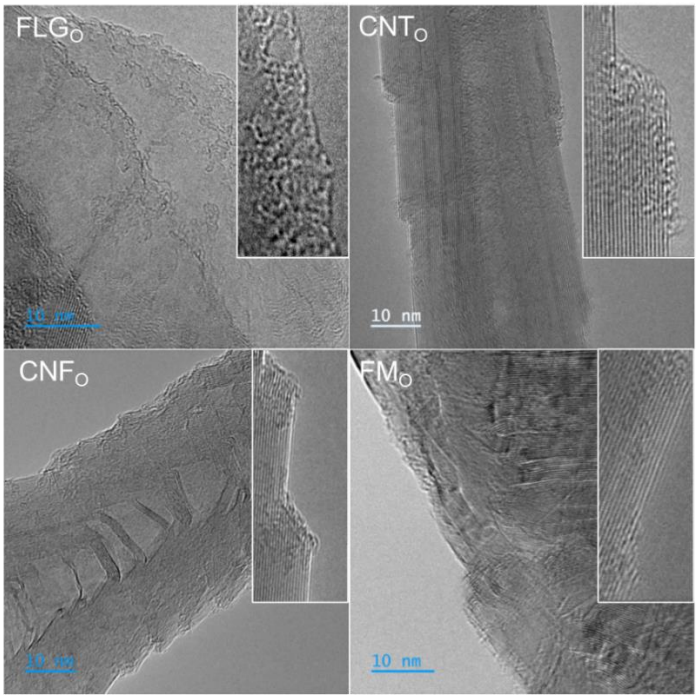

Figure 1. HRTEM micrographs of the four oxidized carbon materials. Scale bar = 10 nm.

Results of Raman and XRD characterization are given in Table 1. Raman spectra are shown in Figure S5 and the main parameters in Table S2. A commonly calculated Raman parameter to probe structural disorder in carbon materials is the ratio between the integrated intensities of the D band (I_D) at ~1380 cm^{-1} (defects of the graphitic structure), and G band (I_G) at ~1580 cm^{-1} (graphitic ordered structure). The FLG_O shows the lower I_D/I_G ratio (low structural disorder), while FM_O shows the higher ratio, CNF_O and CNT_O presenting intermediate values. Compared to the samples heat-treated at 2800 °C, Raman spectroscopy reveals that the D band intensity is strongly affected for FM_O sample while for the others, the change in the ratio of intensities is on average an increase of 0.05. For the FM_O sample, the intensity ratio increases by 0.5 while the FWHM of the G band remains nearly the same (Figure S6). According to Cançado *et al.*,[75] this I_D/I_G increase is due to punctual point defects on the surface with an average distance of L_D = 12 nm between them. The interlayer distance (d_{002}) and the crystallite size value, L_c (stack height of crystallite) and L_a (width of crystallite), were determined by XRD (Table 1). The diffractograms are shown on Figure S7 and the main parameters in Table S3. All materials present a d_{002} close to 0.340 nm, slightly higher than that of perfect graphite (0.335 nm), the lower d_{002} being for FLG_O. FLG_O also shows the larger values for L_c and L_a. The comparison of XRD pattern of the oxidized samples to heat-treated ones shows no significant changes. Classical X-ray analysis was used to address the effect of stacking faults in X-ray diffractograms.[76] FLG_O is composed of Bernal stacked large graphene layers as well as CNF_O. Due to their specific structure CNT_O have a turbostratic stacking. A stacking with AB pairs is present for FM_O. On average, the crystallite size L_c and L_a are slightly reduced. Taken together, the values of d_{002}, L_c and L_a point to a higher crystallinity for FLG_O, which is consistent with the Raman data.

The reactivity of these materials towards air oxidation was probed by TGA (Table 1). The onset decomposition temperature (T_{onset}) of FLG_O is significantly higher than the ones of the other materials. This should be related to the extent of basal surface in FLG_O, which is known to be the less reactive one (*vide infra*). For the three other materials, the onset decomposition temperatures are comparable. Interestingly, the T_{50} (temperature at which 50 % weight loss is reached) of CNF_O and FM_O are significantly higher than the one of CNT_O. Such behavior has already been observed when comparing the oxidation behavior of CNTs and CNFs,[77] and has been attributed to different intrinsic burning properties. Oxidation should be able to proceed very rapidly along the whole sheet of CNTs, in contrast to the fishbone-oriented graphene sheets of CNFs.

Table 1. Textural, structural and surface properties of the four oxidized carbon materials.

Supports	Textural properties		HT-TPD		Raman	XRD			TGA		XPS	
	S_{BET} ($m^2\ g^{-1}$)	V_p ($cm^3\ g^{-1}$)	$S_{non\text{-}basal}$ ($m^2\ g^{-1}$)	$S_{prismatic}$ ($m^2\ g^{-1}$)	I_D/I_G	d_{002} (Å)	L_{c002} (Å)	$L_{a10/100}$ (Å)	T_{onset} (°C)	T_{50} (°C)	C (%)	O (%)
FLG_O	28	0.112	23.2	12.5	0.08	3.37	233	122	701	798	95.9	4.1
CNT_O	144	0.515	80.5	25.2	0.26	3.45	53	88	551	659	95.3	4.7
CNF_O	103	0.321	112.6	57.9	0.29	3.38	115	142	516	738	93.2	6.8
FM_O	64	0.216	76.2	35.5	0.63	3.39	111	144	569	849	92.2	7.8

XPS analyses were performed to probe the surface chemistry of the oxidized carbon materials. Initially, the purity of the materials was verified by the survey scans (Figure S8), which demonstrated that no foreign elements are detected on the surface, with the exception of the FLG_O sample, which contains traces of SiO_x impurities (< 1 at. %). The C 1s spectra (Figure S9) were fitted using 9 components in total, 4 for graphitic/amorphous carbon species, 3 for oxygenated carbon species and 2 for plasmon loss peaks, as assigned in Table S4. Despite the overlap of different carbon species in the C 1s spectra, achieving consistent fitting is possible due to established curve-fitting protocols documented in the literature.[78-80] Based on the fitting results, all materials exhibit a mix of various graphitic/amorphous and oxygenated carbon species, with varying fraction. Specifically, as outlined in Table 2, the FM_O and CNF_O samples show a relatively higher presence of prismatic (layer borders[81]) and oxygenated carbon sites compared to the CNT_O and FLG_O samples, at the expense of graphitic sp^2 carbon. Conversely, the distribution of defect sites appears consistent across all samples. These defective carbon atoms, characterized by lower BE values than graphitic carbon atoms, could stem from intrinsic defects such as vacancies or Stone-Wales defects,[82-84] and/or an increasing number of pentagons within the carbon network.[85,86]

Table 2. Atomic content of the various carbon species resulting from fitting of the C 1s spectra.

Sample	Carbon species (± 2 %)			
	Basal (%)	Prismatic (%)	Defects (%)	OFGs (%)
FLG_O	75	12	5	8
CNT_O	71	14	5	10
CNF_O	69	16	4	11
FM_O	68	15	5	12

Apart from the C 1s peak fitting, the surface oxygen content can be estimated based on the C 1s and O 1s peak intensities. As shown in Table 1, the quantitative analysis confirms the results of the C 1s fitting, showing that CNF_O and FM_O samples have a higher oxygen content. The surface oxygen content follows the order $FLG_O < CNT_O < CNF_O < FM_O$, in accordance with ToF-SIMS analyses. It is noteworthy that the amount of oxygen calculated from the O 1s and C 1s intensities (*i.e.*, peak areas, Table 1) is consistently lower than that found by C 1s peak deconvolution (Table S4). This difference can be attributed to the assumption made in quantitative calculations, which presupposes a homogeneous distribution of oxygen within the carbon matrix. However, as will be demonstrated later, oxygen is predominantly situated at the surface, thus relying on O 1s and C 1s peak intensities for quantitative calculations leads to an underestimation of the oxygen content.

Curve fitting of the O 1s peaks helped to identify three main O 1s components (minimum number of peaks) associated to carbon as well as the O 1s component due to SiO_x in the FLG_O (Figure 2 and Table S5). The components associated to carbon correspond to C=O groups (peak I, 531.4±0.1 eV, including quinone, carbonyl, lactone, and C=O of carboxylic groups), C–OH and/or C–O–C groups (peak II, 533.1±0.1 eV, involving ether and hydroxyl groups bonded to aromatics/aliphatics), and C–OH of carboxylic groups or adsorbed water (peak III, 535.0±0.1 eV).[87-91] No significant variations are observed in the C=O/C–O peak area ratio.

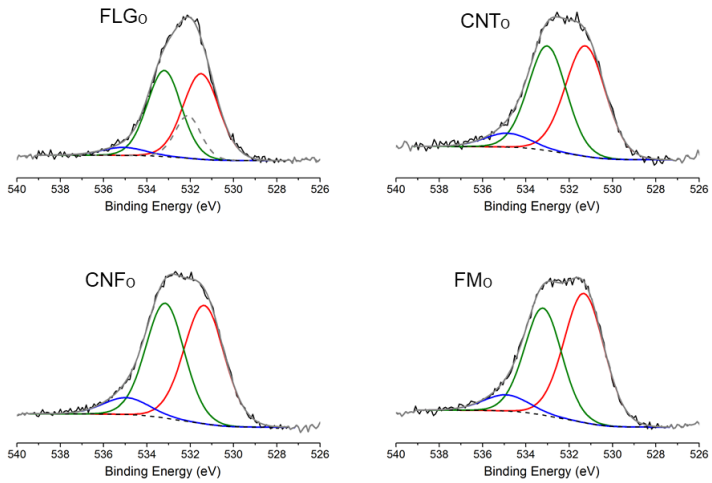

Figure 2. High resolution XPS O 1s spectra of the four graphitic carbons.

The depth distribution of the different carbon species for CNT_O and FM_O samples was addressed through the analysis of C 1s spectra acquired using 4 different photon energies. The use of both laboratory and synchrotron photon sources with incident photons varying between 465 and 1486.6 eV enables non-destructive depth profiling from the outermost surface to the subsurface layers. Estimating the analysis depth as 3 times the inelastic mean free path, the aforementioned measurements correspond to analysis depths between 2.6 and 9.2 nm, respectively.[60] The depth-dependent C 1s spectra of the FM_O sample (Figure S10a) reveal an enhancement of the signal attributed to defects, prismatic, and oxygenated sites in comparison to sp^2 carbon of the basal planes, as the analysis depth decreases. This is clearly demonstrated in Figure S10b, which illustrates the atomic concentration of carbon species as a function of analysis depth. Similar depth distributions were observed for the CNT_O sample (Figure S10c). Overall, the depth-dependent XPS measurements provide solid evidence that defects, prismatic sites and OFGs are predominantly located at the surface, atop the graphitic carbon, irrespective of the sample's carbon structure.

The C KLL Auger peaks are highly sensitive to the relative proportion of sp^2 and sp^3 - hybridized carbon sites in the material. Specifically, the energy difference between the minimum and maximum points of the first derivative of the C KLL spectra, commonly known as the D-parameter, increases from 14 for sp^3 - hybridized carbons (*e.g.*, diamond) to 23 for sp^2 hybridized (*e.g.*, HOPG).[91] In Figure S11, two characteristic examples of C KLL peaks from CNT_O and FM_O are shown before and after derivatization. The calculated D-parameters for all samples are presented in Figure S11c. From this graph, it can be inferred that the D-parameter, and consequently the relative concentration of sp^2 carbon sites, is similar in the FLG_O and FM_O samples, but relatively less compared to CNF_O and CNT_O. The high sp^3 carbon sites content measured for FLG_O might be related to the presence of numerous oxidation debris on this material.

HT-TPD was also used to probe the surface chemistry and quantify the non-basal and edge surface, since this method allows a quantitative evaluation of edges through measurement of evolved gases.[55] Before TPD, the samples were outgassed at 120 °C under high vacuum. TPD profiles and quantifications obtained for all the samples are shown in Figure 3 and Table S6, respectively. CO, CO_2, H_2O and H_2 were detected due to the thermal decomposition of OFGs and H-terminated edge sites. Considering the extremely small amount of evolved gases detected for the heat-treated samples (total gas evolution < 60 μmol g^{-1}),[72] we can assume that all the OFGs and aliphatic -CH groups have been created upon HNO_3 oxidation and/or *via* secondary reactions during the HT-TPD experiment.[92] The oxygen contents (at. %) measured by TPD are lower than the ones measured by XPS. This should thus be related to the fact that TPD analysis probes the bulk sample, whereas XPS is surface-sensitive. Different studies have shown that ether-type oxygen groups were present between the graphitic layers of oxidized CNFs[77] or CNTs.[87] It is therefore very likely that part of the oxygen is bound in between the carbon layers forming ether links between adjacent layers. The FLG_O sample is identified as the material with the lower O content by ToF-SIMS, XPS and TPD, whereas for the other materials the order obtained by TPD is different than that obtained by ToF-SIMS and XPS (Figure S12). This could be an indication of the non-homogeneous distribution of OFGs on the external surface of the materials but also in the bulk or porosity. The HT-TPD spectra of the four oxidized carbon materials shows different CO_2 evolution maxima at ~ 300, 450 and ~ 600 °C, corresponding to the desorption of carboxylic acids, carboxylic anhydrides and lactones, respectively. The evolution of CO_2 at higher temperature might be related to the Boudouard equilibrium.[92] Besides CO_2, a significant amount of water is detected between 150 and 600 °C, which can be correlated to thermally-induced condensation reactions as the ones depicted on Scheme 1.[93]

These can participate in the formation of radicals or carbenes. Considering the fact that the oxidation process was performed in boiling HNO_3, it is improbable that carboxylic anhydrides can be formed under these conditions. Consequently, we propose that their detection by TPD results from their formation by a condensation reaction.

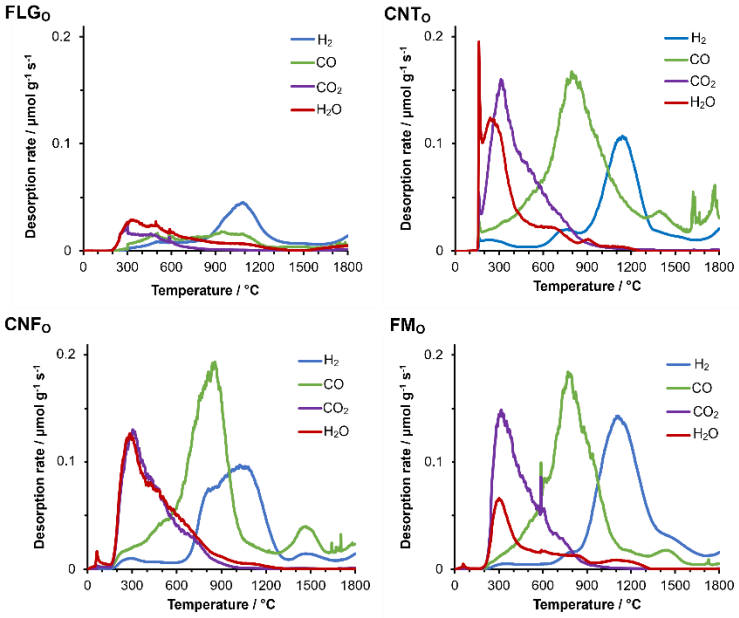

Figure 3. Gas evolution patterns from the four oxidized carbon materials during the HT-TPD measurement up to 1800 °C.

It is worth mentioning that the profiles of water desorption of CNT_O and FM_O differ from the ones of FLG_O and CNF_O (Figure S13). For the former, most of the water desorption stops at T < 500 °C, while for the latter a significant proportion of water continue to desorb up to 900 °C. Considering the condensation reactions presented on Scheme 1, it is probable that the reaction which can results in water evolution at high temperature is the one involving the most stable phenol groups. Therefore, it is possible that samples FLG_O and CNF_O contain more vicinal diols. We also compared the CO_2/H_2O ratio for the four materials and found that this ratio is lower for FLG_O and CNF_O (0.5-1.0) than for CNT_O and FM_O (1.4-2.3). There also, this difference might be related to the spatial distribution of OFGs on the materials. The materials showing a low ratio should present a significant basal surface, which prefers to have OFGs clustered together in a highly ordered fashion.[94] CO evolution is detected in a temperature range from ~ 300 °C to ~ 1200 °C, with the maximum located at ~ 800 °C. This broad signal corresponds to the superposition of the CO evolution associated to the decomposition of carboxylic anhydrides, phenolic, carbonyl (ketones, aldehydes, quinones) and ether (chromene) surface functional groups.[95] The CO emission above 1500 ºC may be derived from the

carboreduction of oxide impurities, such as Na_2O,[96,97] which was the major impurity detected by ToF-SIMS. This high temperature CO evolution is particularly noticeable for the CNF_O sample, which shows the higher sodium content (Figure S1b). Using the total number of edge sites (calculated using the total gas evolution), the surface area of the non-basal sites, $S_{non\text{-}basal}$, can be further calculated.[98] We also calculated the surface area of the H-terminated prismatic sites, $S_{prismatic}$, by using only the H_2 gas evolution (H-terminated edge sites). The values obtained are shown on Table 1. Both XPS and TPD are in reasonable agreement for the evolution of prismatic and non-basal surfaces/carbons for the different samples (Figure S14). The FLG_O samples present the lower prismatic surface and the CNF_O the larger one. Finally, if we consider the amount of water evolved at temperature ≤ 400 °C as a descriptor of the condensation reactions that can results in carbene or radical formation, the following order was obtained: CNT_O (148 μmol g^{-1}) > CNF_O (130 μmol g^{-1}) > FM_O (52 μmol g^{-1}) > FLG_O (24 μmol g^{-1}).

All the analyzes carried out on oxidized materials reveal several points of interest for the study of their thermal defunctionalization aiming at producing carbene or radical type defects. Oxidation makes it possible to eliminate metallic residues from the synthesis catalysts and introduces oxidation debris onto the surface of samples presenting a significant proportion of basal planes (FLG_O and CNT_O). Surface oxygenated groups capable of producing condensation reactions leading to the formation of carbene or radical type sites were detected by XPS and HT-TPD. These groups are mainly present on the surface of the materials but seem to be distributed in a non-homogeneous manner. FLG_O and CNF_O materials, which have a fairly low CO_2/H_2O ratio in HT-TPD, must present zones where these OFGs are clustered. Finally, if we consider the amount of water formed from the condensation reactions at T ≤ 400 °C, the following order was obtained: CNT_O > CNF_O > FM_O > FLG_O.

3.2. Thermal defunctionalization of the oxidized carbon materials. The thermal defunctionalization of the materials was followed by *in-situ* Raman analyses coupled to mass spectrometry, *in-situ* XPS and *ab-initio* molecular dynamics.

For the *in-situ* Raman analyses, the samples were heat-treated under argon from room temperature up to 600 °C. Gas phase analyses by mass spectrometry have confirmed the evolution of CO_2 and H_2O for all the samples in the investigated temperature range (200/400/600 °C, Figure S15). The CO_2/H_2O ratio follows the same trend as for the HT-TPD experiments (higher ratio for CNT_O and FM_O). No significant CO evolution was detected in this temperature range. The spectra of the samples under investigation (Figure S16) consist in several Raman bands such as D, G, D′, G′ (also called as 2D) and D+D′ bands, which are typical of defective graphitic systems. Small temperature-induced frequency shifts were observed in

the 25-600 °C range (Figure S17). No significant variation of the I_D/I_G ratio was observed for FLG_O and CNT_O over the investigated temperature range (Figure S18), pointing to no measurable differences of the disorder in the lattice. In the case of CNF_O and FM_O, their I_D/I_G ratios tend to converge with increasing temperature with a slight increase for CNF_O and a decrease for FM_O. Detailed analysis of the Raman peak intensities in defective graphene have shown that the intensity ratio of the D and D′ peak can be used to get information on the nature of defects.[99] This $I_D/I_{D'}$ ratio is maximum (~13) for sp^3-defects, it decreases for vacancy-like defects (~7), and it reaches a minimum for boundaries in graphite (~3.5). In the present study, the $I_D/I_{D'}$ ratios of the CNT_O, CNF_O and FM_O samples are found to be about 4-5. Based on this, an intermediate value of the $I_D/I_{D'}$ ratio can be reasonably attributed to mixed vacancies and boundary type defects. For FLG_O, the $I_D/I_{D'}$ ratio is lower (~3), in accordance with the low structural disorder of this material. The evolution of the $I_D/I_{D'}$ ratio over temperature is shown on Figure 4. We did not observe a general trend in the evolution of this ratio with temperature. A slight decrease in the $I_D/I_{D'}$ ratio is observed in the case of FLG_O and FM_O, while a slight increase is noted for CNT_O and CNF_O. It is therefore difficult to conclude regarding the introduction of reactive defects by heat treatment from these Raman analyses.

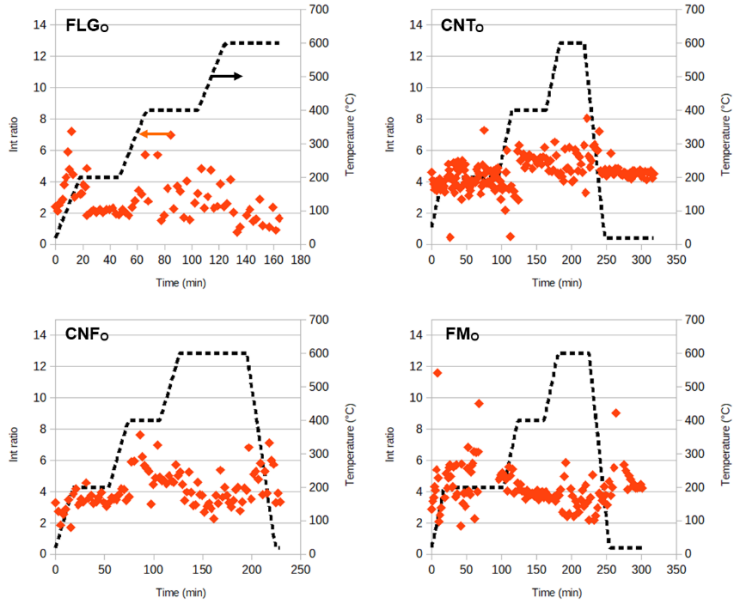

Figure 4. Evolution of the $I_D/I_{D'}$ ratio of the four oxidized carbon materials with temperature.

Synchrotron-based XPS was employed to monitor the surface state of CNT_O and FM_O samples *in situ* during annealing up to 400 °C under high vacuum conditions. The excitation photon energies were selected to record photoelectrons with analysis depths of 2.3 and 4 nm, making

synchrotron-based experiments significantly more sensitive to the surface compared to the laboratory spectra reported in Figure 2 (analysis depth ~7.8 nm). Figure S19 presents the evolution of the oxygen atomic concentration, calculated from the O 1s to C 1s spectra area ratio, as a function of annealing temperature under vacuum. The higher oxygen concentration in Figure S19 compared to Table 1, is attributed to the higher surface sensitivity of the measurements in the former case, indicating that oxygen species are preferentially located at the surface of carbon. This is confirmed by the depth dependent measurements shown in Figure S20, which did not reveal any evident differences in the peak shape at higher analysis depth, apart of a small decrease of the peak at 535 eV attributed to adsorbed water and carboxylic groups. The FM_O sample initially contains a higher amount of oxygen compared to CNT_O, in accordance with the results shown in Table 1. The amount of surface oxygen decreases gradually with increasing annealing temperature for both samples, with a more pronounced decrease observed for FM_O. After annealing at 400 °C, both samples contain very similar amount of adsorbed oxygen species. The O 1s spectra of the two samples at different annealing temperatures are shown in Figure 5.

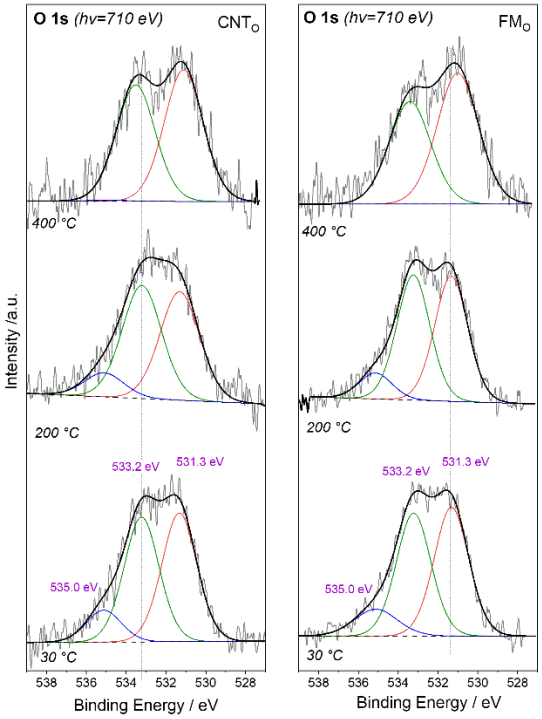

Figure 5. The O 1s photoelectron spectra of CNT_O and FM_O samples as a function of annealing temperature in vacuum measured with 710 eV photon energy.

The results of peak fitting analysis indicate three oxygen species, consistent with the findings from *ex situ* analyzed samples presented in Figure 2. As shown, annealing in vacuum does not

significantly affect the relative fractions of the oxygen species at 531.3 and 533.2 eV, attributed to C=O and C–OH and/or C–O–C groups, respectively. For both samples, a slight decrease of the contribution of the C–OH and/or C–O–C groups relative to the C=O groups is noticed. In contrast, the peak around 535 eV decreases with temperature, disappearing entirely at 400 °C, which is consistent with the desorption of water and decomposition of carboxylic groups upon annealing at this temperature. The slight decrease of the contribution of the C–OH and/or C–O–C groups could be explained by the reaction pathways depicted on Scheme 1, which involved reactions of vicinal C–OH and COOH groups and decomposition of C–O–C groups.

We now turn our attention to the C 1s peak, the analysis of which shows the evolution of the carbon sites with annealing temperature. As shown in Figure 6, which present the results of pick fitting analysis, the concentration of both basal and defect carbon sites increases with annealing temperature, at the expense of oxygenated and prismatic species.

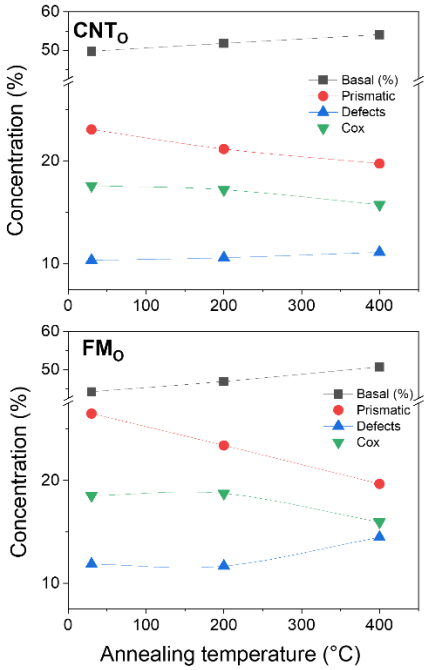

Figure 6. The evolution of the various carbon sites derived from the fitting of the C 1s spectra recorded with 465 eV photon energy.

A decrease of OFGs (mainly carboxylic groups) with a concomitant increase of defect sites is what is expected from condensation reactions (Scheme 1). However, it is important to note that the changes in the fraction of carbon sites do not necessarily correspond to their mutual transformation since the annealing temperature in the *in-situ* experiment is relatively low. Instead, these changes may also arise from an enhanced signal of a carbon sites, due to the high

surface sensitivity of synchrotron-XPS. This enhancement occurs following the desorption of oxygen species that were previously over these sites. Thus, the results of Figure 6 suggests that adsorbed oxygen species (water and carboxylic groups) on basal sites preferentially desorb upon annealing compared to oxygen adsorbed on prismatic carbon sites.

Since thermal defunctionalization can induce an evolution of the type and concentration of OFGs on the support, we also rely on molecular dynamics simulations to study the atomistic structure of progressively heated material. As a carbon material with a disordered structural surface similar to the experimentally used oxidized CNTs or FLGs, a model of O-functionalized graphene was considered presenting a high level of basal surface and, consequently, a low level of prismatic surface. Specifically, it contains oxygen functionalities such as ethers, carbonyls/quinones, lactones and carboxyls, although it does not contain hydroxyl/phenolic groups to avoid some of the side reactions shown in Scheme 2 (even if some of them are reactions of interest).

To investigate the correlation between the time evolution propagated by the model system at the *ab initio* level and the experimental one, four molecular dynamics simulations of the carbon material are performed at different heating rates for a temperature range from 0 to 1800 K (ca. 1500 °C to represent the experimental conditions). The MD trajectory at 20 K ps^{-1} is summarized in Figure 7, being propagated for a sufficiently long time period (90 ps) to allow a higher energy balance among all degrees of freedom, while the trajectories at 200 (9 ps), 100 (18 ps), and 50 (36 ps) K ps^{-1} are given in Figure S21, Figure S22, and Figure S23, respectively. MD are presented as potential energy; therefore, kinetic energy is not considered to distinguish energy fluctuations derived from possible rearrangements of existing functional groups (since MDs have a constant progression of temperature, the kinetic contribution scales monotonically and can be omitted from the analysis). As can be seen in Figure 7a, the average energy is relatively constant up to approximately 300 °C, from which the system tends to stabilize (energy downhill), first slowly up to about 600 °C and remains constant again up to 800 °C. Then it rapidly goes up to about 1100 °C to finally becomes relatively constant up to the final 1500 °C. These intervals are largely caused by the most significant structural changes produced on the graphitic material, which are the breaking of C–C bonds eliminating carboxylic motifs in the form of molecular carbon dioxide, which reorganizes the material recovering aromaticity. The atomic structures corresponding to each CO_2 release are detailed in Figure 7b. The slower stabilization interval is consistent with the single decarboxylation reaction around 500 °C (38 ps simulation time), while up to four CO_2 losses at about 800 °C (54 ps), 950 °C (61 ps), 1050 °C (66 ps) and 1150 °C (71 ps) are prompted in the faster stabilization interval. However, the

chemical decomposition caused by heating to high temperatures in the absence of oxygen involves further chemical composition changes.

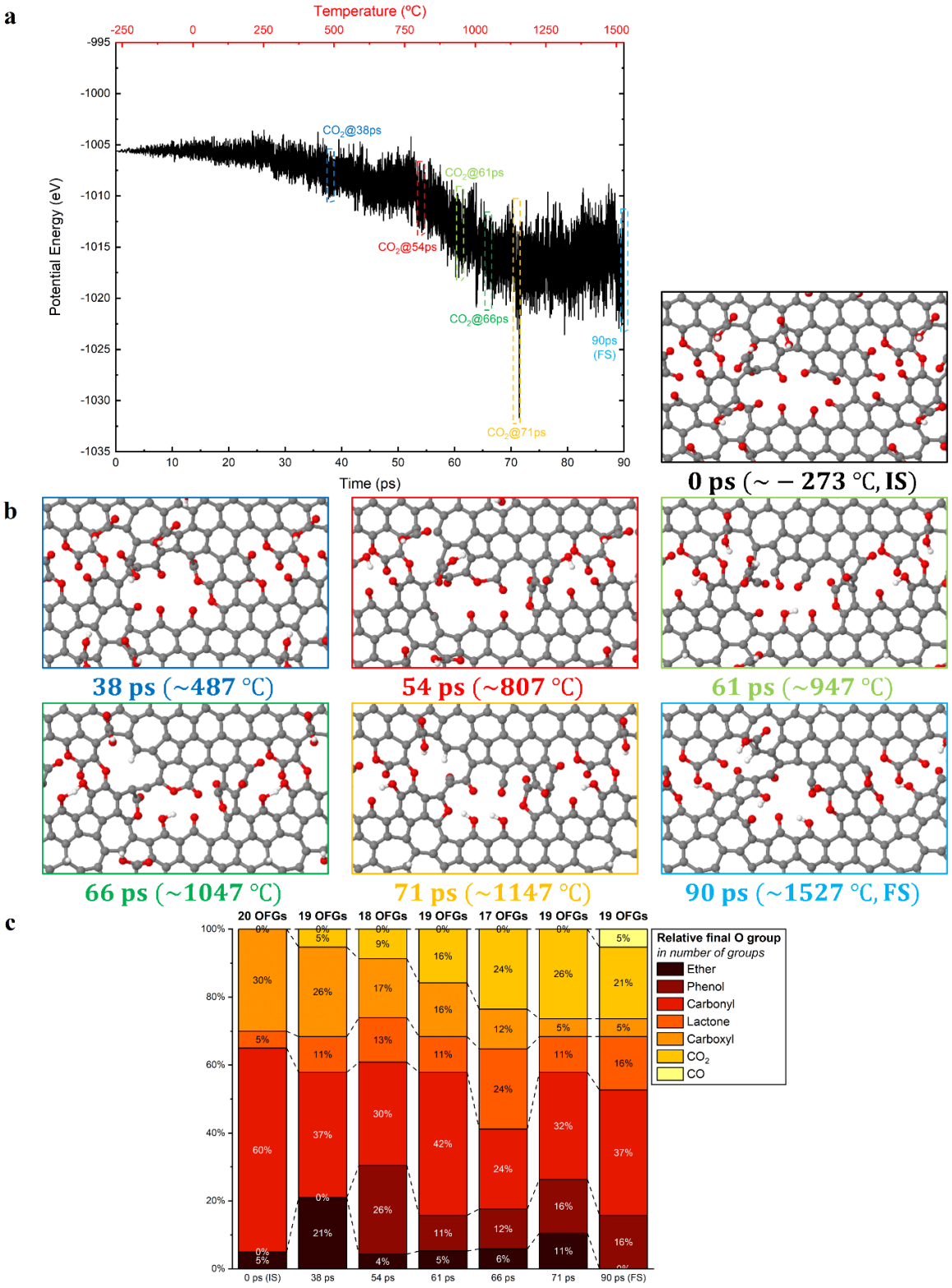

Figure 7. AIMD of the carbon model (**a**), initial and successive (including final) structure after each release of CO_2 (**b**), and evolution of OFG concentration (**c**) at heating rate of 20 K ps^{-1}. Oxygen, carbon, and hydrogen atoms are colored candy apple red, Philippine gray, and white, respectively.

The temporal evolution of the concentration for the main OFGs is depicted in Figure 7c. Initially, the carbon support functionalities are mostly limited by carbonyl groups and to a lesser extent carboxyl groups, together with minor ether and lactone groups. As expected, the carboxyl groups are progressively decomposed as the CO_2 molecules are formed. As a result, hydrogen atoms connected to -COOH units are reincorporated into the material in different ways, among which the reduction of C=C double bonds of the carbon network to saturated C–H and of polar carbonyl-type multiple bonds to phenols stand out. It could explain the gradual drop of C=O bonds as well as the appearance of C–OH bonds.[30] In addition, a significant increase in lactone groups is noted throughout the simulation, derived from the insertion of some carbonyl in ether functions above 1000 °C. Minor rearrangements, such as the formation of furan rings (by intramolecular cyclization between nearby carbonyls) and two- and three-atom carbon chains (induced by ring openings in the presence of carbonyls), are also observed occasionally.[100] Finally, it is interesting to highlight the presence of molecular CO in the final structure, promoted by the abstraction of oxygen from CO_2 by the highly reactive carbon sites that arise during thermal defunctionalization, which further illustrates the dynamic nature of these physicochemical processes. The high reducing power of reactive carbon sites could be preserved by limiting their interactions in this type of reaction, for example, by removing *in situ* the released gaseous species (essentially H_2O and CO_2).

However, for a given simulation temperature, the studied heating rates had a noticeably unequal effect on the main oxygen groups functionalizing the carbon material model. The concentration of the different OFGs in the initial (at 0 K) and final structures (at 1800 K) of each of the studied MD trajectories is given in Figure S24. Compared to the fastest heating rate, carried out at 200 K ps^{-1}, the O-functionalized graphene is barely decarboxylated, producing very few modifications such as the reduction of carbonyl motifs to phenol. But at intermediate heating rates, such as at 100 and 50 K ps^{-1}, more evident changes are experienced by the model graphene. Almost all of the decarboxylation reaction took place, which pushed the loss of CO_2. As a consequence, a greater amount of C=O groups is reduced into C–OH ones. Finally, it can be seen how the slower heating rate, run at 20 K ps^{-1}, continued to elucidate the progressive decrease in carbonyl groups, in addition to the transformations explained previously for this last situation, which would support the experimental observations.

On the other hand, as in the TPD spectra exemplified in Figure 3, each type of O-containing surface groups on carbon materials thermally decomposes at different temperatures, depending on the thermal stability of the groups. For carboxylic acids, the observed temperature is typically between 200 and 500 °C and is well documented in the literature.[93,101] These studies

usually demonstrate that -COOH groups with varying acidities decompose at distinct temperatures, with the strongest acidic group undergoing decomposition at the highest temperature. It has been suggested that these differences in acidity may be attributed to the presence of carbonyl or ether functional groups in the *meta* or *ortho* position, which could contribute to lowering the pKa value.[101] Notwithstanding this observation, a discussion of the chemical environment, in a broader sense, of surface carboxylic acid groups could not be found in the literature. However, it is reasonable to hypothesize that the chemical environment can have a significant impact on the strength of the C–C bond that is broken to form CO_2 and thus on the reaction mechanism (*i.e.*, molecular or radical). Thermal decomposition of benzoic acid, used to model surface carboxylic acids on coal, is the only *in silico* mechanistic investigation of the decarboxylation reaction.[102,103] Direct and stepwise decarboxylation pathways *via* hydrogen migration from -CO_2H to *ipso*-C and *ortho*-C, respectively, have been identified as plausible (Figure S25). In contrast, the unimolecular stepwise radical process appears to be an unlikely mechanism, as it would require overcoming a significant energy barrier for homolytic cleavage of the CO_2–H bond. It should be noted, however, that this model does not account for the complex surface chemistry of carbon materials. In particular, the carboxylic acid groups present on the basal plane are orthogonal and therefore not conjugated to the π system of the carbon material, which differs from the benzoic acid model. Furthermore, the proximity of OFGs to carboxylic acids could play a role in the decarboxylation mechanism and thereby modify the chemical reaction pathway.

In the propagated MD simulations, beyond undergoing a decarboxylation reaction upon heating, these carboxyl groups showed a relationship between the chronological order and the temperature at which they are removed as a function of the heating rate. The temperature dependence of the successive release of COOH to form CO_2 in the O-functionalized graphene model at the studied heating rates is illustrated in Figure 8a. As the heating rate slows, the decarboxylation reactions mostly take place earlier, with the first ejection appearing below 500 °C at 20 K ps^{-1}. Furthermore, from the third in the case of 100 K ps^{-1} and from the second in the case of 50 and 20 K ps^{-1}, the CO_2 releases could be considered almost linearly dependent on temperature, allowing extrapolation towards the complete removal of carboxylic acids. Despite this, it might be necessary to continue lowering the heating rates to, for example, 5 or 10 K ps^{-1} to further accelerate the removal of all carboxyl groups and approach the observed experimental temperature range. Nevertheless, these results would enhance the fact that the slowest heating rates are the ones that best describe, in our case, the experimental evidence.

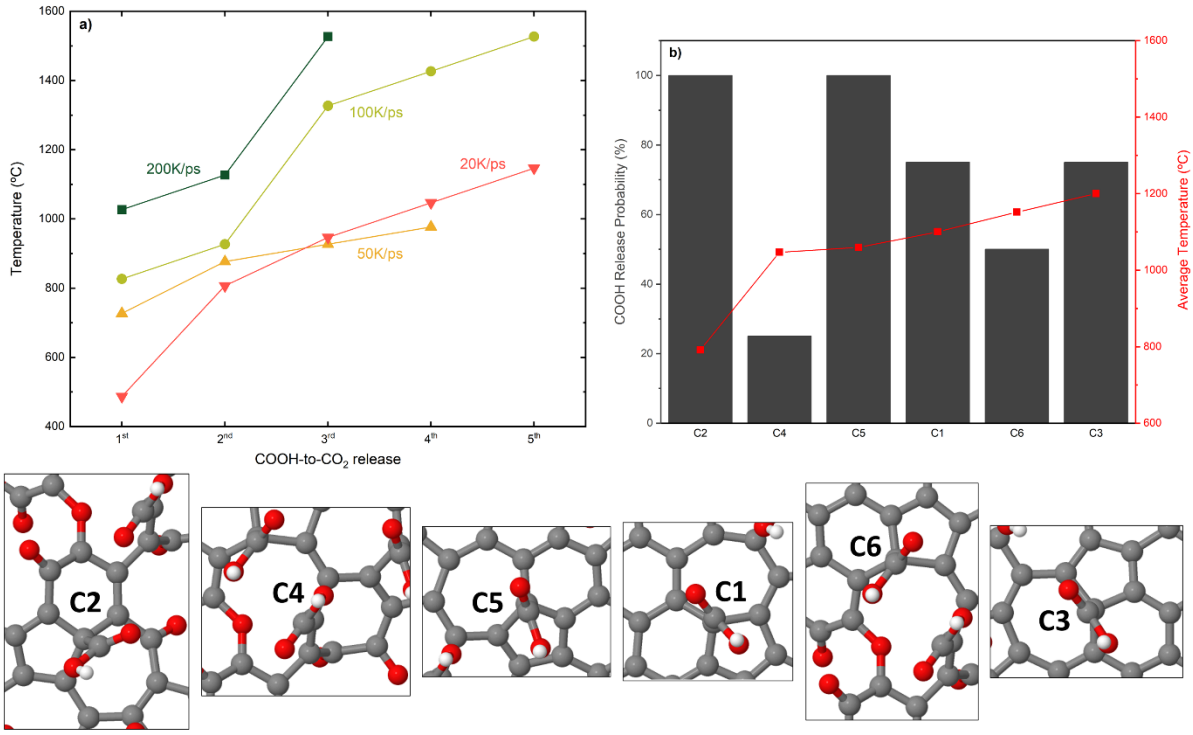

Figure 8. (**a**) Temperature dependence of the successive release of COOH forming CO_2 in the O-functionalized graphene model at heating rates of 200 (pearl green), 100 (acid green), 50 (marigold) and 20 (salmon orange) K ps^{-1}, and (**b**) probability and average temperature of release for each chemically-independent surface carboxyl group of the system from the propagated MD simulations (corresponding structures are below as insets).

Simultaneously, the functionalized graphene model includes, from the structural point of view, up to six COOH motives (anchored between five-, six- and seven-membered ring rearrangements originating from Stone-Wales defects) with unique coordination environments, the rest being arranged by translational symmetry. Although not all of them are ejected as has been noted, disregarding the complete decarboxylation of the material at 1500 °C. Therefore, which ones are released from the carbon lattice more easily and which ones remain attached during the thermal process are tracked, allowing to assess possible stability/instability patterns between the carboxylic acids and the surface. From the complete MD simulations, the probability that each chemically independent surface carboxyl group of the system is reduced to CO_2, ordered according to its corresponding average temperature, is shown in Figure 8b. Clearly, the group labeled C2 is the least stable and, therefore, the easiest to release, since its probability is highest (it occurred in all simulations) and the average temperature is the lowest (it is usually the first to be ejected). In the coordination environment, the five-carbon ring remains pristine, while the six- and seven-carbon rings are connected to two and one oxygen functionality, respectively. From here, the average temperature increases prominently by about

250 °C and continues to grow gradually, although the probability of releasing the other COOHs does not show an obvious trend. Among them, the C4 group seems to be one of the most stable and most difficult to release, promoted by the placement between a seven-carbon ring with a quinone (double carbonyl function) and a wide ten-membered ring with an ether and another carboxylic acid. In addition, the location only on two carbon rings shows that the carbon supporting the COOH is partially unsaturated, which reinforces its superior bond strength.

To rationalize the increased stability of the C4 carboxylic acid, the *C*–*C*OOH bond lengths of the six coordinatively unique carboxylic acids of the carbon material are measured. For each of the four simulations performed, these measurements are taken at the initial state (0 ps of MD) and after each CO_2 release (*e.g.*, for the heating rate of 20 K ps^{-1}, at 38, 54, 61, 66, and 71 ps of MD). The resulting data are presented in Figure S26 and Table S7, with a 95% confidence interval for each mean distance. The most stable C4 carboxylic group is the one with the shortest $C_{support}$–C_{acid} bond, averaging only 1.49 Å. Furthermore, the C5 group, which is one of the most likely to be released, has the longest and, therefore, weakest bond, at 1.63 Å. However, the low thermal stability of the C2 carboxylic group cannot be explained by the *C*–*C*OOH bond length. In this case, the presence of two carbonyl groups in the proximity of C2 could potentially be responsible for the stabilization of the radical formed upon decarboxylation.[104] It is also noteworthy that the -CO*O*–*H* bond length of C2 (Figure S26 and Table S7) is significantly shorter than that of the other carboxylic acids, which correlates well with the previous observation that weaker carboxylic acids are the most thermally labile. Importantly, a negative correlation between the measured pK_a of substituted benzoic acids and the *C*–*C*OOH bond lengths is reported by Ishikita *et al.*,[105] confirming that benzoic acid is not an appropriate model of surface carboxylic groups present on the basal plane.

In conclusion, probing the thermal defunctionalization of these materials at the atomistic level constitutes a challenging task, as many reactions involving different types of OFGs can occur. However, the results obtained by *in situ* XPS point towards a decrease in carboxylic surface groups upon defunctionalization with a concomitant increase in defect sites, which is expected from condensation reactions. In addition, the presence of highly reactive carbon sites arising during thermal defunctionalization is shown by *ab initio* molecular dynamics simulations. These results suggest that the generation of electronically unsaturated carbon sites upon thermal defunctionalization should be feasible.

3.3. Magnetic properties. As stated in the introduction, some properties, such as the chemical reactivity or magnetic properties of graphitic carbons are usually attributed to their structural disorder and the presence of unpaired electrons. Non-contaminated and relatively ordered

carbon-based structures as HOPG show a large diamagnetic susceptibility.[106] For defective carbon materials, paramagnetism has been demonstrated, with contribution from point defects, edges or chemical doping.[107,108] VSM and EPR spectroscopy are two commonly used techniques for evaluating the magnetic properties of carbon materials and providing insights into the spin properties, which are far from fully understood and still controversial. In recent years, dynamic nuclear polarization (DNP) has also been used to study paramagnetic centers in carbon materials, and to distinguish between different unpaired electron centers on the carbon surface.[109,110]

The electronic and magnetic properties of the four oxidized carbon materials were investigated by VSM and EPR before and after thermal defunctionalization. Magnetic susceptibility measurements were used to determine the number of unpaired electron spins (N_{spin}) in these samples. Magnetic susceptibility measurements were conducted to determine N_{spin} of each material. Figure 9 shows the magnetic susceptibility between 5 K and 300 K after field cooling, for the oxidized materials before and after thermal defunctionalization at 400 °C. The oxidized carbons which have been thermally defunctionalized are labeled C_{O+TD}. When unpaired electrons exist in carbon materials, the magnetic susceptibility derived from the unpaired electron spins is inversely proportional to temperature according to the Curie-Weiss law (Curie paramagnetism). All the materials show strong diamagnetism on the whole temperature range at high temperatures with an additional Curie-like paramagnetic contribution at low temperatures (except for FLG). Note that CNT_O, CNF_O and FM_O one peak is observed in susceptibility for the different samples at around 70 K, rather constant in position. The presence of such a peak has already been reported for graphitic carbons, and it has been attributed to the effect of O_2,[111] or metallic impurities.[112] The presence of such a peak, which was not due to solidified oxygen was also observed in sulfur-doped amorphous carbons.[113,114] For the thermally defunctionalized samples, which have been measured without air exposure, this peak disappear for CNF_O and FM_O and is dramatically reduced for CNT_O, which could be due to the effect of heating procedure on removing impurities. Note that if the thermally defunctionalized sample is exposed to air after a first measurement, this peak appears in the second one. The obtained room temperature mass diamagnetic susceptibilities χ are -122, -52, -51 and -55×10^{-9} m^3 kg^{-1} for FLG_O, CNT_O, CNF_O and FM_O, respectively, in agreement with reported values of graphitic materials presenting large anisotropy in the susceptibility. After thermal defunctionalization, all the materials show a diamagnetic response, and they χ values are -121, -55, -59 and -61×10^{-9} m^3 kg^{-1} for FLG_{O+TD}, CNT_{O+TD}, CNF_{O+TD} and FM_{O+TD}, respectively.

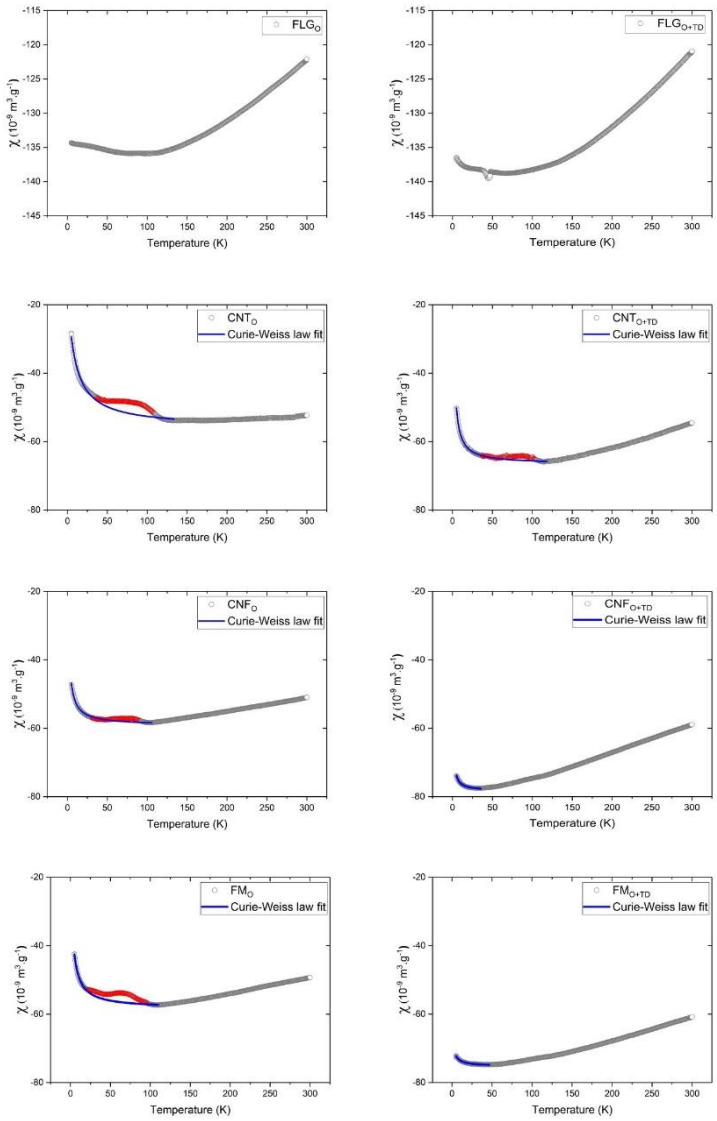

Figure 9. Magnetic susceptibility between 5 K and 300 K after field cooling, recorded at 5T for the oxidized, and thermally defunctionalized carbon materials and fitted by Curie-Weiss law at low temperatures (5 K-120 K, blue line).

The paramagnetic response at low temperature is predicted by the Curie-Weiss law, allowing to extract the values of N_{spin} for the carbons before and after thermal defunctionalization (Table 3 and Figure 9 for fitting). Thermal defunctionalization results in an appreciable decrease in N_{spin}. This decrease is more notable in the case of CNTs (~70 % decrease) than for CNFs and FM (~45 % decrease). The evolution of the magnetic properties has been determined by the measurement of the magnetic moments as a function of the applied magnetic field at 300 and 5 K. The resulting data are displayed on Figure S27 and Figure S28, for the oxidized and thermally defunctionalization materials, respectively. The general behavior is dominated by the expected diamagnetic response of ordered carbon materials characterized by a negative slope, without any traces of ferromagnetism.

Table 3. Properties estimated from magnetic susceptibility measurement and EPR for the four oxidized carbon materials before and after thermal defunctionalization.

Sample	N_{spin} ($\times 10^{19}$ g^{-1})	
	VSM (Curie-Weiss law)	EPR
FLG_O	-	2.3
FLG_{O+TD}	-	1.2
CNT_O	5.6	4.2
CNT_{O+TD}	1.8	3.5
CNF_O	1.1	2.1
CNF_{O+TD}	0.6	2.2
FM_O	1.0	2.4
FM_{O+TD}	0.6	2.2

Continuous-wave EPR experiments performed on carbon materials usually provide spectra with complicated linewidths presenting both narrow and broad components related to the presence of localized and conduction electrons, and their interplay.[115] The mobile conduction electrons in graphitic carbon particles presenting dimensions larger than the microwave penetration depth (skin depth, $\delta > 3$ μm) conduct to a Dysonian line shape with broad linewidth. When the skin depth becomes larger than the particle size, this behavior can be disrupted, the Dysonian line shape giving its place to a Lorentzian. If conduction electrons are confined in very small particles with weak contacts among them a Gaussian component appears. The localized electrons resulting from the interruption of the π-system, which can interact with the mobile conduction electrons, exhibit a Lorentzian line shape with a narrow linewidth. Finally, non-interacting localized electrons, like in radicals, with small hyperfine interactions, exhibit a Gaussian line shape with a very narrow linewidth.

Room-temperature EPR spectra and simulations of the four oxidized carbon materials before and after thermal defunctionalization are presented in Figure 10.

Large decreases of the cavity Q-values upon sample insertion were recorded for all materials, confirming electrical conductivity. We note that the small L_a values determined from XRD studies on all materials (see above) are in agreement with the total absence of Dysonian line shapes, both of which point to particle sizes that are small compared to the skin depth. All materials give relatively broad line widths (1-4 mT_{pp}). This should be mainly related to the presence of numerous delocalized π-electrons on their surface, which broaden the EPR signals and to the low mobility of the electrons in the conduction band that would otherwise induce motional narrowing. All materials give a signal at around $g = 2$, typical of carbon radicals. Simulations allowed us to extract the different contributions (relevant parameters are given in Table 4).

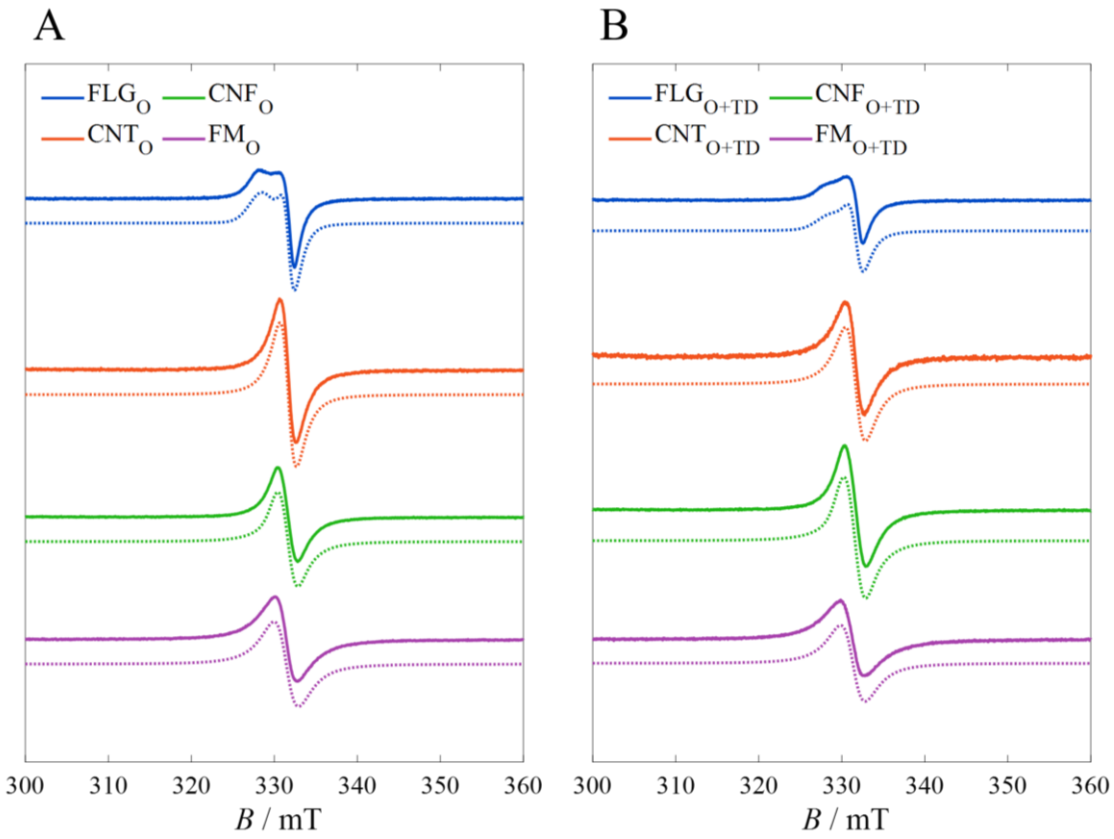

Figure 10. Experimental (solid) and simulated (dashed) EPR spectra of the four oxidized carbon materials before (A) and after (B) thermal defunctionalization at 300 °C. Spectra were recorded at room temperature in sealed tubes under a helium atmosphere, with parameters given in experimental section and simulation parameters given in Table 4. The microwave frequency was around 9.312 GHz for FLG samples, 9.314 GHz for CNT samples and 9.311 GHz for CNF and FM samples. Spectra are normalized by the number of scans.

FLG_O exhibits a signal with two components: one with a Lorentzian line shape centered at $g = 2.0056$ (σ_{pp} = 1.5 mT), and one with a Gaussian line shape centered at g = 2.016 (σ_{pp} = 3.4 mT). Deconvolution of the spectra are shown in Figure S29. We have attributed the Lorentzian contribution to localized electrons, either from the edges or from O-decorated areas, interacting with delocalized π-electrons; and the Gaussian contribution to the delocalized π-electrons in FLG_O crystallites (L_c = 23 nm, L_a = 12 nm).[72] Interestingly, CNF_O also exhibits a signal with two components: a major component centered at g = 2.0046 with a Lorentzian line shape, and a minor one, with a contribution of only 10 %, centered around g = 2.0076 with a Gaussian line shape. The two other materials show spectra with Lorentzian line shapes only. All spectra could be fitted with one species around g = 2.007 and different linewidths attributable to the intrinsic delocalized (conducting) π electrons in the graphite sheets. It appears from this analysis of the line shapes of the four materials that, as in the case of reduced graphene oxide,[116] the major contribution to the EPR signal arises from localized π-defect states strongly

coupled with itinerant spins within the sp^2 framework. Globally, there is no pronounced effect of the defunctionalization on the line shapes and *g* factors.

Table 4. Simulation parameters for the EPR spectra of the four heat-treated graphitic carbons. Simulations were done using Easyspin.[117] σ_{Gpp} et σ_{Lpp} are peak-to-peak Gaussian and Lorentzian line widths, respectively. Asterisks denote samples that gave *p*-EPR spectra.

Sample	g_{iso}	σ_{Gpp} (mT)	σ_{Lpp} (mT)	% of species
FLG_O	2.0056(5)	0	1.53(6)	58(2)
	2.0165(5)	3.43(8)	0	42(2)
FLG_{O+TD}	2.0051(6)	0	1.77(3)	74(10)
	2.0165(5)	3.37(11)	0	26(10)
CNT_O	2.0065(15)	0	1.99(1)	100
CNT_{O+TD}*	2.0066(15)	0	2.41(2)	100
CNF_O	2.0047(5)	0	2.69(3)	92(1)
	2.0076(5)	2.01(2)	0	8(1)
CNF_{O+TD}*	2.0047(5)	0	2.69(3)	90(1)
	2.0078(5)	2.24(2)	0	10(1)
FM_O	2.0072(5)	0	2.96(2)	100
FM_{O+TD}*	2.0075(5)	0	3.30(2)	100

N_{spin} can also be determined from the EPR measurement by comparison to the spectrum of a standard sample with known spin concentration, measured under identical conditions (see Materials and Methods). Although the absolute values of the N_{spin} obtained by VSM at low temperature and EPR at room temperature are not the same, the observed tendency for the increasing of N_{spin}, $CNT_O > CNF_O \approx FM_O$ is the same, confirming the reliability of the two methods. Thermal defunctionalization results in an appreciable decrease in N_{spin} for FLG (~50 % decrease) and CNTs (~37 % decrease), while the N_{spin} of CNFs and FM is not significantly impacted. This result might be consistent with the proposal that the defects and OFGs are associated with the appearance and stabilization of unpaired spins.[18] However, considering the 8 samples, no clear correlation was obtained between N_{spin} and the oxygen content determined by HT-TPD, neither with the H content, with the total gas evolved, or with the surface of edges as proposed in ref. [98] (Figure S30). Nevertheless, the results obtained suggest that two groups of materials present different behavior. For FLG and CNT supports the correlation between these parameters and N_{spin} is reasonable. For CNFs and FM, these parameters cannot be correlated to N_{spin}. Although a good correlation between S_{edge} and N_{spin} has been reported for carbon materials showing high OFG concentration, we have recently shown that both the $S_{prismatic}$ and the S_{basal} should be taken into account to rationalize the N_{spin} in materials showing low $S_{prismatic}$,[72] as the ones of the present study.

We also rely on pulse EPR (*p*-EPR) methods that allow the separation of the signals of different species, depending on their spin relaxation (Figure 11). Thus, species with short relaxation time, as conduction electrons, are undetectable by *p*-EPR, whereas edge and molecular states can be detected.[118]

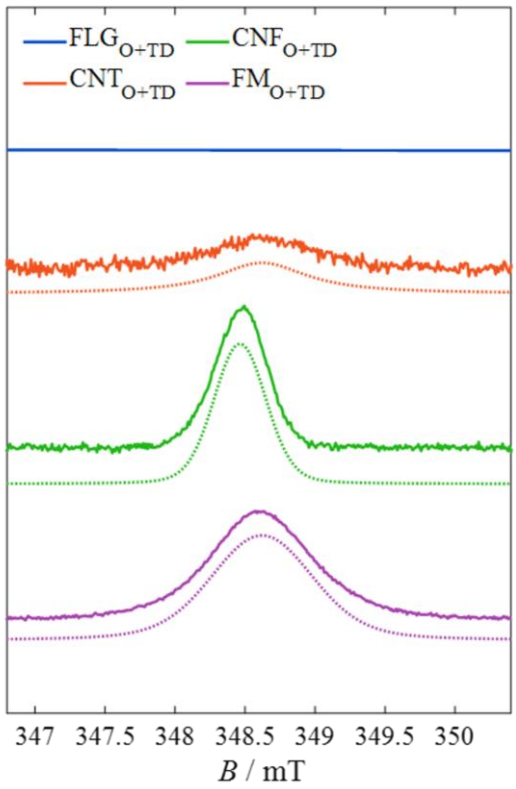

Figure 11. Experimental (solid) and simulation (dashed) echo detected field sweep of the four heated at 2800 °C and oxidized graphene materials after defunctionalization at 300 °C for 2 hours. Spectra were recorded at 20 K with parameters given in experimental section. Spectra are normalized to the number of scan and the number of shot per point. The microwave frequency was around 9.737 GHz for FLG_{O+TD} and CNT_{O+TD} and around 9.734 GHz for CNF_{O+TD} and FM_{O+TD}. Simulation parameters are given in Table S8.

We observe that the line widths of the species detected by *p*-EPR (Table S8) are around an order of magnitude smaller than those detected by *cw*-EPR. Such narrow peaks should normally be detected in *cw*-EPR experiments assuming comparable quantities. Their non-observation in *cw*-EPR leads us to suggest that they are minor species whose *cw*-EPR signals are masked by those of the major species with broader lines. Thus, the two types of spectra give complementary information: the dominant contributions observed by *cw*-EPR cannot be observed by *p*-EPR, and by *p*-EPR we can detect and identify low-intensity components that could not be resolved in the *cw*-EPR spectrum. It was shown that the paramagnetic centers observed in the spin echo constitute a small fraction of those observed in the *cw*-EPR spectrum.

Preliminary relaxation studies allowed us to determine T_1 and T_M times for the defunctionalized materials (Figure S31, Figure S32, and Table S9). Indeed, echo decay experiments showed a stretched exponential decay without ESEEM (Electron Spin Echo Envelope Modulation) contribution, while saturation recovery experiments also showed a stretched-exponential spin-lattice relaxation. Moreover, we note that signals appearing in *p*-EPR spectra are only those originating from samples that were defunctionalized by thermal treatment at 300 °C for 2 h. These samples did not exhibit *p*-EPR signal prior to defunctionalization, which means that these minor species were in fact produced during the defunctionalization treatment.

Taken together, the VSM and EPR results therefore suggest that the two materials whose N_{spin} decreases the most after thermal defunctionalization are FLG and CNTs. These two materials are those which present the lowest prismatic surface and the lowest concentration of OFGs (Table 1). In fact, a very good correlation was determined between the decrease of N_{spin} upon defunctionalization determined by EPR and the prismatic surface and oxygen content in the samples (Figure S33). The observed tendency for the decreasing of N_{spin} in the defunctionalized samples is $CNT_{O+TD} > FLG_{O+TD} \approx CNF_{O+TD} \approx FM_{O+TD}$. Finally, echo-detected field-swept EPR spectra show the apparition of a signal only upon thermal defunctionalization, particularly for samples showing a high proportion of prismatic surface. On such surface, it is expected that the vicinity of OFGs should favor the condensation reactions depicted in Scheme 2, which should result in the generation of electronically unsaturated carbon sites.

3.4. Catalytic properties. The catalytic activity of the four oxidized carbon materials before and after thermal defunctionalization was evaluated for the catalytic dehydrogenation of indoline to indole (Figure 12a).[119] This reaction can operate in the presence (oxidative dehydrogenation) or not (acceptorless dehydrogenation) of oxygen on metal-free catalysts, including with carbocatalysts.[98,120,121] However, the mechanism of oxidative dehydrogenation on carbocatalysts is still disputable and inconclusive. Some mechanistic studies on N-doped carbons have shown that the oxidative dehydrogenation of N-heterocycles was a radical reaction process; and superoxide ($\bullet O^{2-}$) and hydroxyl radical (•OH) were probed as the reductive oxygen species.[121] Other authors have proposed that, different from metal catalyst, the reaction on N-doped or N/P-co-doped carbon proceeds *via* a non-free radical pathway.[122,123] On oxidized carbon materials, quinoidic groups were proposed to be the active sites, on which the rate-determining H-abstraction step can occurs either by direct bimolecular hydride transfer or *via* an hemiaminal pathway.[124] Oxidized carbons, such as graphene oxide, can also produce stable carbon radicals under photo-irradiation, which are active for indoline dehydrogenation under air.[125] In fact, depending on the carbon material, different active sites have been proposed,

on which the reaction is completed such as clustered N sites,[120] OFGs or unpaired electrons in carbon edge sites.[98,121] All these sites being able to activate O_2.

The performance of the four oxidized carbon materials before and after thermal defunctionalization was evaluated at 100 °C in xylene for 5 hrs. The reaction hardly proceeded in the absence of catalyst (conversion = 7.5 %). Whatever the type of carbon material, the conversion is decreasing after thermal defunctionalization. This result is not consistent with a study by Helaja *et al.*, where it was shown that thermal decarboxylation of oxidized carbons improves the activity of the catalyst.[124] The decrease in conversion follows the order: CNTs (39.5%) ~ FLG (36%) > FM (27.5 %) ~ CNFs (26 %).

The effect of thermal defunctionalization on conversion is more pronounced on CNT and FLG, as it was the case for the N_{spin}. This could suggest a direct correlation between N_{spin} and indoline conversion. However, no clear and direct correlation could be draw considering the 8 samples (Figure S34a). A closer inspection of the results obtained reveals again two groups of materials showing different behavior. First, FLG and CNT samples, for which the correlation between conversion and N_{spin} is reasonable (Figure S34b). Then, CNFs and FM, for which conversion cannot be correlated to N_{spin}. As OFGs (epoxy, hydroxyl, ketonic and carboxyl groups) have been identified as active sites for O_2 activation and/or H-abstraction,[124,126,127] we also consider a possible correlation between the conversion and the O content determined by HT-TPD. The similarity of figures Figure S34b and Figure S30b suggests that such correlation could be good. Indeed, a good correlation was observed between the indoline conversion and the O content (Figure 12b). Since the nature of the oxygen-containing gases emitted during TPD (CO_2, H_2O and CO) is related to the type of OFGs present on the surface, we also tried to correlate the conversion to the type of gas emitted (Figure S35). Although reasonable correlations were obtained with the amount of CO or CO_2 evolved, the best correlation was definitively obtained taken into account the total amount of gas evolved (CO_2 + CO + H_2O). This latter correlation is not compatible with the fact that a single type of active site operates for the reaction. As both neutral (for example ketonic carbonyl groups[128]) or radical active sites have been proposed for oxidative dehydrogenation on carbon materials, we conducted a radical inhibition experiment with the most active CNT_O catalyst. When the radical scavenger 2,6-di-tert-butyl-4-methylphenol (BHT) was added, the conversion of indoline decreases systematically of ten points for each sampling, which correspond to 12-30% decrease (Figure S36). Reproducibility tests were independently performed to verify that this decrease in conversion was not within the reproducibility of the experiments. The limited variation of conversion in the presence of 2 equivalents of BHT and the good correlation obtained between the conversion and the oxygen

content determined by HT-TPD indicate that the main reaction pathway should not imply free radical sites (carbon- or oxygen-centered), but OFGs.

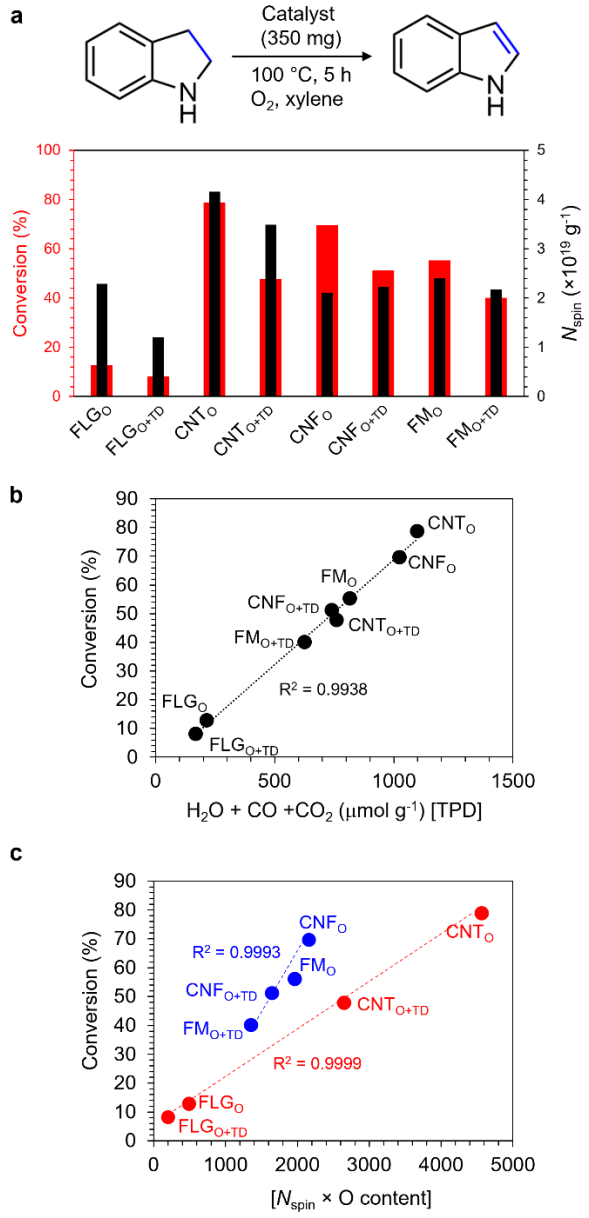

Figure 12. a The relationship between N_{spin} and conversion of indoline. **b** Correlation between the oxygen content determined by HT-TPD and the conversion of indoline. For the four oxidized carbon materials after thermal defunctionalization, was consider only the content of oxygen release at T > 400°C. **c** Correlation between a parameter integrating the oxygen content determined by HT-TPD and the N_{spin} and the conversion of indoline.

Since radicals may still be involved in the reaction, even if to a small extent, and since no clear correlation has been established between conversion and N_{spin} but between conversion and oxygen content, we also considered a possible correlation between conversion and a parameter integrating N_{spin} and O content. No clear and direct correlation could be draw considering the 8

samples (Figure 12c). However, if we consider independently the two groups of materials previously discussed (FLG and CNT on one side and CNF and FM on the other side), we noticed a very good correlation between indoline conversion and the [N_{spin} x O content].

If we compare the materials showing a value of [N_{spin} × O content] approximately equal (CNF_O and CNT_{O+TD}), we see that the most active material (CNF_O) is the one that has the higher O content and not N_{spin}. If we compare two materials presenting similar conversion (CNF_{O+TD} and CNT_{O+TD}) we see that despite the N_{spin} differ significantly between these two samples (higher for CNT_{O+TD}), the O content is similar for both materials. If we compare two materials that have similar N_{spin} (CNF_O and FM_{O+TD} or FM_O and CNF_{O+TD}) we see that the higher conversion is obtained with the material showing the larger O content. We are therefore leaning towards a non-radical mechanism that prevails for indoline dehydrogenation on these carbocatalysts.

The fact that CNF and FM samples exhibit better conversion than FLG and CNTs for a given [N_{spin} × O content] domain should be related to their structure. These materials are the one showing the higher proportion of prismatic surface. We therefore proposed that the prismatic surface should favors the formation of a denser network of OFGs compared to the basal surface.[94] As suggested by the echo-detected field-swept EPR spectra, this denser network should be more favorable to the formation from vicinal OFGs of localized electronic states that might be involved in the reaction. This denser network should also favor the existence of specific sites containing two functionalities (quinone, lactone, anhydride) [129] that might be involved in the reaction.

4. CONCLUSIONS

We have investigated the effect of thermal defunctionalization (300-400 °C under inert atmosphere) on the structural, chemical and magnetic properties of four graphitized and oxidized carbons presenting different prismatic and basal surfaces (FLG_O, CNT_O, CNF_O and FM_O). This treatment was performed with the aim of producing stabilized localized electronic states from condensation reactions, which have been proposed to impact the magnetic properties and chemical reactivity of carbon materials.

Our results show that the oxidation treatment makes it possible to eliminate metallic residues (ToF-SIMS analyses), which may affect both magnetic chemical and properties. XPS and ToF-SIMS analyses agree with the following order for the surface oxygen content: $FLG_O < CNT_O < CNF_O < FM_O$. The graphitized materials with the higher percentage of prismatic surface area show the higher oxygen content when oxidized. Surface OFGs capable of producing condensation reactions have been detected by XPS and HT-TPD. These groups (carboxylic and

phenol), predominantly situated at the surface, seem to be distributed in a non-homogeneous manner. Annealing under an inert atmosphere induces the decrease of carboxylic surface groups with a concomitant increase of defect sites (*in situ* XPS analyses). Such a behavior is expected from condensation reactions. *Ab initio* molecular dynamic simulations have highlighted the complex surface chemistry that can occur during this thermal defunctionalization step. VSM and EPR analyses show that the spin density globally decreases upon thermal defunctionalization. However, *p*-EPR analyses evidence that new paramagnetic centers are created upon defunctionalization, particularly for samples showing a high proportion of prismatic surface. This result validates our approach. However, the contribution of electronically unsaturated carbon sites to the chemical reactivity for the dehydrogenation of indoline is only moderate, for which the surface OFGs are the main active sites.

AUTHOR INFORMATION

Corresponding Author

*E-mail: philippe.serp@ensiacet.fr

ORCID

Mathieu Vidal: https://orcid.org/0009-0008-8430-9035

Maryam S. Dehaghani: https://orcid.org/0009-0009-0744-9883

Javier Navarro-Ruiz: https://orcid.org/0000-0002-3604-9338

Takeharu Yoshii: https://orcid.org/0000-0002-1869-6021

Keigo Wakabayashi: https://orcid.org/0009-0007-7098-944X

Hirotomo Nishihara: https://orcid.org/0000-0003-4497-4248

Mathias Barreau: https://orcid.org/0000-0002-1917-134X

Fabrice Bournel: https://orcid.org/0000-0001-6452-3415

Jérôme Volkman: https://orcid.org/0000-0001-7108-7682

Guillaume Clet: https://orcid.org/0000-0001-5999-5880

Spyridon Zafeiratos: https://orcid.org/0000-0001-8165-2585

Nolwenn Le Breton: https://orcid.org/0000-0002-5638-9444

Pascal Puech: https://orcid.org/0000-0002-9863-0128

Iann C. Gerber: orcid.org/0000-0001-5091-2655

Athanassios K. Boudalis: https://orcid.org/0000-0002-8797-1170

Thomas Blon: https://orcid.org/0000-0002-1177-4787

Philippe Serp: orcid.org/0000-0003-1424-2724

Author Contributions

M. Vidal: Investigation, Formal analysis, original draft Writing; M. S. Dehaghani: Investigation, Formal analysis, original draft Writing; J. Navarro-Ruiz: Investigation, Formal analysis, original draft Writing, Writing – review & editing; T. Yoshii: Investigation, Formal analysis, original draft Writing; K. Wakabayashi: Investigation; H. Nishihara: Formal analysis, Writing – review & editing; M. Barreau: Investigation; F. Bournel: Investigation, Formal analysis; J. Volkman: Investigation, Formal analysis, original draft Writing; G. Clet: Investigation, Formal analysis, original draft Writing; Writing – review & editing; S. Zafeiratos: Investigation, Formal analysis, original draft Writing; Writing – review & editing; N. Le Breton: Investigation, Formal analysis, original draft Writing; P. Puech: Formal analysis, Writing – review & editing; I. Gerber: Investigation, Formal analysis, original draft Writing; A. K. Boudalis: Formal analysis, Writing – review & editing; T. Blon: Formal analysis, Writing – review & editing; P. Serp: Project administration, Funding acquisition, original draft Writing, Writing – review & editing. The manuscript was written through contributions of all authors. All authors have given approval to the final version of the manuscript.

Funding Sources

This work has received funding from the French Agence Nationale de la Recherche under grant agreement ANR-21-CE07-0021 (GRAAL). This work was supported by JST PRESTO grant no. JPMJPR23QA.

Notes

The authors declare no competing financial interest.

Supporting Information. ToF-SIMS analyses; TEM/HRTEM micrographs; Raman spectra, associated parameters and I_D/I_G ratio; XRD diffractograms and associated parameters; XPS spectra, fitting parameters and data; Auger spectra; gas evolution during the HT-TPD; evolution of C/O ratio; evolution of prismatic and non-basal surfaces from HT-TPD; evolution of CO_2 and H_2O; evolution of the frequency of the G and D bands; evolution of the I_D/I_G ratio; atomic oxygen concentration; molecular dynamics simulations at heating rates of 200, 100, and 50 K ps^{-1}; concentration of different oxygen functional groups; thermal decarboxylation reaction of benzoic acid; C–COOH and -COO–H bond lengths of the six different carboxylic acids and corresponding data; magnetic hysteresis loops; spectral deconvolution of EPR spectra; correlation curves; simulation parameters for the pulse EPR spectra; echo decay traces obtained

by pulse EPR; saturation recovery traces obtained by pulsed EPR; relaxation times measured by echo decay and saturation recovery; indoline conversion.

ACKNOWLEDGMENTS

J.N.-R. and I.C.G. acknowledge the computer resources through the "Calcul en Midi-Pyrénées" initiative CALMIP (projects p0812), and CINES, IDRIS, and TGCC under the allocation 2023-A0140906649 made by GENCI. The French research infrastructure INFRANALYTICS FR2054 is acknowledged for its support.

REFERENCES

(1) Fitzer, E. Book Review: Chemistry and Physics of Carbon, Vol. 1 and 2. Edited by P. L. Walker jr. *Angew. Chem. Int. Ed.* **1967,** *6* (12), 1092.

(2) Tuček, J.; Błoński, P.; Ugolotti, J.; Swain, A. K.; Enoki, T.; Zbořil, R. Emerging chemical strategies for imprinting magnetism in graphene and related 2D materials for spintronic and biomedical applications. *Chem. Soc. Rev.* **2018,** *47* (11), 3899.

(3) Navalon, S.; Dhakshinamoorthy, A.; Alvaro, M.; Garcia, H. Carbocatalysis by Graphene-Based Materials. *Chem. Rev.* **2014,** *114* (12), 6179.

(4) Miyamoto, Y.; Nakada, K.; Fujita, M. First-principles study of edge states of H-terminated graphitic ribbons. *Phys. Rev. B* **1999,** *59* (15), 9858.

(5) Komeily-Nia, Z.; Qu, L.-T.; Li, J.-L. Progress in the Understanding and Applications of the Intrinsic Reactivity of Graphene-Based Materials. *Small Sci.* **2021,** *1* (2), 2000026.

(6) Yeh, C.-N.; Chai, J.-D. Role of Kekulé and Non-Kekulé Structures in the Radical Character of Alternant Polycyclic Aromatic Hydrocarbons: A TAO-DFT Study. *Sci. Rep.* **2016,** *6* (1), 30562.

(7) Wu, D.; Gao, X.; Zhou, Z.; Chen, Z. In *Graphene Chemistry*, John Wiley & Sons, Ltd, **2013**, https://doi.org/10.1002/9781118691281.ch3.

(8) Martin, J. W.; Pascazio, L.; Menon, A.; Akroyd, J.; Kaiser, K.; Schulz, F.; Commodo, M.; D'Anna, A.; Gross, L.; Kraft, M. π-Diradical Aromatic Soot Precursors in Flames. *J. Am. Chem. Soc.* **2021,** *143* (31), 12212.

(9) Kyotani, T.; Ozaki, J.-i.; Ishii, T. What can we learn by analyzing the edge sites of carbon materials? *Carbon Rep.* **2022,** *1* (4), 188.

(10) Radovic, L. R. Probing the 'elephant': On the essential difference between graphenes and polycyclic aromatic hydrocarbons. *Carbon* **2021**, *171*, 798.

(11) Radovic, L. R.; Bockrath, B. On the Chemical Nature of Graphene Edges: Origin of Stability and Potential for Magnetism in Carbon Materials. *J. Am. Chem. Soc.* **2005,** *127* (16), 5917.

(12) He, K.; Lee, G.-D.; Robertson, A. W.; Yoon, E.; Warner, J. H. Hydrogen-free graphene edges. *Nat. Commun.* **2014,** *5* (1), 3040.

(13) Gerber, I.; Oubenali, M.; Bacsa, R.; Durand, J.; Gonçalves, A.; Pereira, M. F. R.; Jolibois, F.; Perrin, L.; Poteau, R.; Serp, P. Theoretical and Experimental Studies on the Carbon-Nanotube Surface Oxidation by Nitric Acid: Interplay between Functionalization and Vacancy Enlargement. *Chem. - Eur. J.* **2011,** *17* (41), 11467.

(14) Ishii, T.; Kashihara, S.; Hoshikawa, Y.; Ozaki, J.-i.; Kannari, N.; Takai, K.; Enoki, T.; Kyotani, T. A quantitative analysis of carbon edge sites and an estimation of graphene sheet size in high-temperature treated, non-porous carbons. *Carbon* **2014,** *80*, 135.

(15) Pentsak, E. O.; Gordeev, E. G.; Ananikov, V. P. Carbocatalysis: From Acetylene Trimerization to Modern Organic Synthesis. A Review. *Dokl. Phys. Chem.* **2020,** *493* (2), 95.

(16) Berdonces-Layunta, A.; Lawrence, J.; Edalatmanesh, S.; Castro-Esteban, J.; Wang, T.; Mohammed, M. S. G.; Colazzo, L.; Peña, D.; Jelínek, P.; de Oteyza, D. G. Chemical Stability of (3,1)-Chiral Graphene Nanoribbons. *ACS Nano* **2021,** *15* (3), 5610.

(17) Lawrence, J.; Berdonces-Layunta, A.; Edalatmanesh, S.; Castro-Esteban, J.; Wang, T.; Jimenez-Martin, A.; de la Torre, B.; Castrillo-Bodero, R.; Angulo-Portugal, P.; Mohammed, M. S. G.et al. Circumventing the stability problems of graphene nanoribbon zigzag edges. *Nat. Chem.* **2022,** *14* (12), 1451.

(18) Jung, S.-M.; Park, J.; Shin, D.; Jeong, H. Y.; Lee, D.; Jeon, I.-Y.; Cho, H.; Park, N.; Yoo, J.-W.; Baek, J.-B. Paramagnetic Carbon Nanosheets with Random Hole Defects and Oxygenated Functional Groups. *Angew. Chem. Int. Ed.* **2019,** *58* (34), 11670.

(19) Augustyniak-Jabłokow, M. A.; Tadyszak, K.; Strzelczyk, R.; Fedaruk, R.; Carmieli, R. Slow spin relaxation of paramagnetic centers in graphene oxide. *Carbon* **2019,** *152*, 98.

(20) Vorobiev, A. K.; Astvatsaturov, D. A.; Fionov, A. V.; Chumakova, N. A. Paramagnetic centers in graphite oxide according to EPR spectra and DFT calculations. *Chem. Phys. Lett.* **2020,** *754*, 137722.

(21) Krasheninnikov, A. V.; Banhart, F. Engineering of nanostructured carbon materials with electron or ion beams. *Nat. Mater.* **2007,** *6* (10), 723.

(22) Savage, R. H. Process of making chemically active graphitic carbon powder. General Electric Co: US2601953A, **1949**.

(23) Kiciński, W.; Dyjak, S. Transition metal impurities in carbon-based materials: Pitfalls, artifacts and deleterious effects. *Carbon* **2020,** *168*, 748.

(24) Menéndez, J. A.; Phillips, J.; Xia, B.; Radovic, L. R. On the Modification and Characterization of Chemical Surface Properties of Activated Carbon: In the Search of Carbons with Stable Basic Properties. *Langmuir* **1996,** *12* (18), 4404.

(25) Chen, C.-M.; Zhang, Q.; Yang, M.-G.; Huang, C.-H.; Yang, Y.-G.; Wang, M.-Z. Structural evolution during annealing of thermally reduced graphene nanosheets for application in supercapacitors. *Carbon* **2012,** *50* (10), 3572.

(26) Chernyak, S. A.; Ivanov, A. S.; Strokova, N. E.; Maslakov, K. I.; Savilov, S. V.; Lunin, V. V. Mechanism of Thermal Defunctionalization of Oxidized Carbon Nanotubes. *The J. Phys. Chem. C* **2016,** *120* (31), 17465.

(27) Gabe, A.; Baba, T.; Hirahara, T.; Mikami, T.; Oda, N.; Miyata, Y.; Kawata, K.; Otake, Y. Quantifying Carbon Active Sites Chemisorbing Hydrogen on Oxygen Containing Activated Carbons during Heat Treatment in Hydrogen Atmosphere. *Langmuir* **2023,** *39* (40), 14284.

(28) Baba, T.; Gabe, A.; Hirahara, T.; Mikami, T.; Oda, N.; Kawata, K.; Otake, Y. Unraveling Thermal Stability of Carbon Active Sites Chemisorbing Hydrogen on Oxygen-Containing Activated Carbons. *The J. Phys. Chem. C* **2024,** *128* (24), 9981.

(29) Phillips, J.; Kelly, D.; Radovic, L.; Xie, F. Microcalorimetric Study of the Influence of Surface Chemistry on the Adsorption of Water by High Surface Area Carbons. *J. Phys. Chem. B* **2000,** *104* (34), 8170.

(30) Kolev, S. K.; Aleksandrov, H. A.; Atanasov, V. A.; Popov, V. N.; Milenov, T. I. Surface chemistry of reduced graphene oxide: H-atom transfer reactions. *Appl. Surf. Sci.* **2021,** *567*, 150815.

(31) Qiu, W.; Chen, C.-C.; Xu, L.; Cui, L.; Paul, D. R.; Koros, W. J. Sub-Tg Cross-Linking of a Polyimide Membrane for Enhanced CO2 Plasticization Resistance for Natural Gas Separation. *Macromolecules* **2011,** *44* (15), 6046.

(32) Du, N.; Dal-Cin, M. M.; Robertson, G. P.; Guiver, M. D. Decarboxylation-Induced Cross-Linking of Polymers of Intrinsic Microporosity (PIMs) for Membrane Gas Separation. *Macromolecules* **2012,** *45* (12), 5134.

(33) Montoya Sánchez, N.; de Klerk, A. Oxidative Ring-Opening of Aromatics: Decomposition of Biphenyl Carboxylic Acids and Zinc Biphenyl Carboxylates. *Energy Fuels* **2015,** *29* (12), 7910.

(34) Winter, K.; Barton, D. The thermal decomposition of benzoic acid. *Can. J. Chem.* **1970,** *48* (24), 3797.

(35) Elmas Kimyonok, A. B.; Ulutürk, M. Determination of the Thermal Decomposition Products of Terephthalic Acid by Using Curie-Point Pyrolyzer. *J. Energ. Mater.* **2016,** *34* (2), 113.

(36) Kim, T. Y.; Baek, J.; Song, C. K.; Yun, Y. S.; Park, D. S.; Kim, W.; Han, J. W.; Yi, J. Gas-phase dehydration of vicinal diols to epoxides: Dehydrative epoxidation over a Cs/SiO_2 catalyst. *J. Catal.* **2015,** *323*, 85.

(37) De Ras, K.; Kusenberg, M.; Thybaut, J. W.; Van Geem, K. M. Unraveling the carbene chemistry of oxymethylene ethers: Experimental investigation and kinetic modeling of the high-temperature pyrolysis of OME-2. *Proc. Combust. Inst.***2023,** *39* (1), 125.

(38) Neĭman, M. B.; Kovarskaya, B. M.; Golubenkova, L. I.; Strizhkova, A. S.; Levantovskaya, I. I.; Akutin, M. S. The thermal degradation of some epoxy resins. *J. Polym. Sci.* **1962,** *56* (164), 383.

(39) Menzel, R.; Tran, M. Q.; Menner, A.; Kay, C. W. M.; Bismarck, A.; Shaffer, M. S. P. A versatile, solvent-free methodology for the functionalisation of carbon nanotubes. *Chem. Sci.* **2010,** *1* (5), 603.

(40) Hu, S.; Chen, S.; Menzel, R.; Goode, A. D.; Ryan, M. P.; Porter, A. E.; Shaffer, M. S. P. Aqueous dispersions of oligomer-grafted carbon nanomaterials with controlled surface charge and minimal framework damage. *Faraday Discuss.* **2014,** *173* (0), 273.

(41) Hu, S.; Laker, Z. P. L.; Leese, H. S.; Rubio, N.; De Marco, M.; Au, H.; Skilbeck, M. S.; Wilson, N. R.; Shaffer, M. S. P. Thermochemical functionalisation of graphenes with minimal framework damage. *Chem. Sci.* **2017,** *8* (9), 6149.

(42) Lin, D.; Futaba, D. N.; Kobashi, K.; Zhang, M.; Muroga, S.; Chen, G.; Tsuji, T.; Hata, K. A Microwave-Assisted, Solvent-Free Approach for the Versatile Functionalization of Carbon Nanotubes. *ACS Nano* **2023,** *17* (4), 3976.

(43) Rivera-Cárcamo, C.; Scarfiello, C.; García, A. B.; Tison, Y.; Martinez, H.; Baaziz, W.; Ersen, O.; Le Berre, C.; Serp, P. Stabilization of Metal Single Atoms on Carbon and TiO_2 Supports for CO_2 Hydrogenation: The Importance of Regulating Charge Transfer. *Adv. Mater. Interfaces* **2021,** *8* (8), 2001777.

(44) Yang, Q.; Liu, H.; Yuan, P.; Jia, Y.; Zhuang, L.; Zhang, H.; Yan, X.; Liu, G.; Zhao, Y.; Liu, J.et al. Single Carbon Vacancy Traps Atomic Platinum for Hydrogen Evolution Catalysis. *J. Am. Chem. Soc.* **2022,** *144* (5), 2171.

(45) Yang, X.; Xia, H.; Qin, X.; Li, W.; Dai, Y.; Liu, X.; Zhao, M.; Xia, Y.; Yan, S.; Wang, B. Correlation between the vacancy defects and ferromagnetism in graphite. *Carbon* **2009,** *47* (5), 1399.

(46) Weber, J. R.; Koehl, W. F.; Varley, J. B.; Janotti, A.; Buckley, B. B.; Van de Walle, C. G.; Awschalom, D. D. Quantum computing with defects. *PNAS* **2010,** *107* (19), 8513.

(47) Carr, L. D.; Lusk, M. T. Graphene gets designer defects. *Nat. Nanotechnol.* **2010,** *5* (5), 316.

(48) Aly, A. H.; Sayed, F. A.; Elsayed, H. A. Defect mode tunability based on the electro-optical characteristics of the one-dimensional graphene photonic crystals. *Appl. Opt.* **2020**, *59* (16), 4796.

(49) Aguillon, F.; Borisov, A. G. Atomic-Scale Defects Might Determine the Second Harmonic Generation from Plasmonic Graphene Nanostructures. *J. Phys. Chem. Lett*. **2023**, *14* (1), 238.

(50) Duley, W. W. Polycyclic aromatic hydrocarbons, carbon nanoparticles and the diffuse interstellar bands. *Faraday Discuss.* **2006,** *133* (0), 415.

(51) Ghigo, G.; Maranzana, A.; Tonachini, G.; Zicovich-Wilson, C. M.; Causà, M. Modeling Soot and Its Functionalization under Atmospheric or Combustion Conditions by Density Functional Theory within Molecular (Polycyclic-Aromatic-Hydrocarbon-like) and Periodic Methodologies. *J. Phys. Chem. B* **2004,** *108* (10), 3215.

(52) Gerber, I. C.; Serp, P. A Theory/Experience Description of Support Effects in Carbon-Supported Catalysts. *Chem. Rev.* **2020,** *120* (2), 1250.

(53) Rivera-Cárcamo, C.; Serp, P. Single Atom Catalysts on Carbon-Based Materials. *ChemCatChem* **2018,** *10* (22), 5058.

(54) Yu, W.; Yoshii, T.; Aziz, A.; Tang, R.; Pan, Z.-Z.; Inoue, K.; Kotani, M.; Tanaka, H.; Scholtzová, E.; Tunega, D.et al. Edge-Site-Free and Topological-Defect-Rich Carbon Cathode for High-Performance Lithium-Oxygen Batteries. *Adv. Sci.* **2023,** *10* (16), 2300268.

(55) Xia, T.; Yoshii, T.; Nomura, K.; Wakabayashi, K.; Pan, Z.-Z.; Ishii, T.; Tanaka, H.; Mashio, T.; Miyawaki, J.; Otomo, T.et al. Chemistry of zipping reactions in mesoporous carbon consisting of minimally stacked graphene layers. *Chem. Sci.* **2023,** *14* (32), 8448.

(56) Ait Ali, B.; Bouhmouche, A.; Wendling, L.; Hu, C.; Bouillet, C.; Schmerber, G.; Saeedi, A. M.; Zafeiratos, S.; Papaefthimiou, V.; Moubah, R.et al. Impact of film thickness on

the structural, linear and non-linear optical properties of ferroelectric Bi_2FeCrO_6 perovskite thin films. *Vacuum* **2023,** *216*, 112411.

(57) Chen, D.; Zhang, J.; Barreau, M.; Turczyniak-Surdacka, S.; Joubert, O.; La Salle, A. L. G.; Zafeiratos, S. Ni-doped CeO_2 nanoparticles to promote and restore the performance of Ni/YSZ cathodes for CO_2 electroreduction. *Appl. Surf. Sci.* **2023,** *611*, 155767.

(58) Paloukis, F.; Papazisi, K. M.; Balomenou, S. P.; Tsiplakides, D.; Bournel, F.; Gallet, J. J.; Zafeiratos, S. In situ X-ray photoelectron spectroscopy study of complex oxides under gas and vacuum environments. *Appl. Surf. Sci.* **2017,** *423*, 1176.

(59) Fairley, N.; Fernandez, V.; Richard-Plouet, M.; Guillot-Deudon, C.; Walton, J.; Smith, E.; Flahaut, D.; Greiner, M.; Biesinger, M.; Tougaard, S.et al. Systematic and collaborative approach to problem solving using X-ray photoelectron spectroscopy. *Appl. Surf. Sci. Advances* **2021,** *5*, 100112.

(60) Smekal, W.; Werner, W. S. M.; Powell, C. J. Simulation of electron spectra for surface analysis (SESSA): a novel software tool for quantitative Auger-electron spectroscopy and X-ray photoelectron spectroscopy. *Surf. Interface Anal.* **2005,** *37* (11), 1059.

(61) Mosse, I. S.; Sodisetti, V. R.; Coleman, C.; Ncube, S.; de Sousa, A. S.; Erasmus, R. M.; Flahaut, E.; Blon, T.; Lassagne, B.; Šamořil, T.et al. Tuning Magnetic Properties of a Carbon Nanotube-Lanthanide Hybrid Molecular Complex through Controlled Functionalization. *Molecules* **2021,** *26* (3), 563.

(62) Kresse, G.; Furthmüller, J. Efficiency of ab-initio total energy calculations for metals and semiconductors using a plane-wave basis set. *Comput. Mater. Sci.* **1996,** *6* (1), 15.

(63) Kresse, G.; Furthmüller, J. Efficient iterative schemes for ab initio total-energy calculations using a plane-wave basis set. *Phys. Rev. B* **1996,** *54* (16), 11169.

(64) Perdew, J. P.; Burke, K.; Ernzerhof, M. Generalized Gradient Approximation Made Simple. *Physical Review Letters* **1996,** *77* (18), 3865.

(65) Grimme, S.; Antony, J.; Ehrlich, S.; Krieg, H. A consistent and accurate ab initio parametrization of density functional dispersion correction (DFT-D) for the 94 elements H-Pu. *J. Chem. Phys.* **2010,** *132* (15).

(66) Blöchl, P. E. Projector augmented-wave method. *Phys. Rev. B* **1994,** *50* (24), 17953.

(67) Kresse, G.; Joubert, D. From ultrasoft pseudopotentials to the projector augmented-wave method. *Phys. Rev. B* **1999,** *59* (3), 1758.

(68) Navarro-Ruiz, J.; Rivera-Cárcamo, C.; Machado, B.; Serp, P.; Del Rosal, I.; Gerber, I. C. Computational Design of Pd Nanoclusters and Pd Single-Atom Catalysts Supported on O-Functionalized Graphene. *ACS Appl. Nano Mater.* **2021,** *4* (11), 12235.

(69) Monkhorst, H. J.; Pack, J. D. Special points for Brillouin-zone integrations. *Phys. Rev. B* **1976,** *13* (12), 5188.

(70) Makov, G.; Payne, M. C. Periodic boundary conditions in ab initio calculations. *Phys. Rev. B* **1995,** *51* (7), 4014.

(71) Nosé, S. A molecular dynamics method for simulations in the canonical ensemble. *Mol. Phys.* **1984,** *52* (2), 255.

(72) Vidal, M.; Dehaghani, M. S.; Yoshii, T.; Wakabayashi, K.; Cameán, I.; Barreau, M.; Le Breton, N.; Gerber, I. C.; Puech, P.; Boudalis, A. K.et al. Probing Prismatic/Basal Surfaces of Carbon Materials upon Graphitization by Gas Adsorption, TPD, and XPS. *The J. Phys. Chem. C* **2024**, *128* (44), 18993–19012.

(73) de Lima, A. H.; Scarpa, I.; Azevedo, N. C. L.; Lelis, G. C.; Strauss, M.; Martinez, D. S. T.; Furlan de Oliveira, R. Oxidative debris in graphene oxide: a decade of research. *J. Mater. Chem. C* **2023,** *11* (37), 12429.

(74) Chen, X.; Chen, B. Direct Observation, Molecular Structure, and Location of Oxidation Debris on Graphene Oxide Nanosheets. *Environ. Sci. Technol.* **2016,** *50* (16), 8568.

(75) Gustavo Cançado, L.; Gomes da Silva, M.; Martins Ferreira, E. H.; Hof, F.; Kampioti, K.; Huang, K.; Pénicaud, A.; Alberto Achete, C.; Capaz, R. B.; Jorio, A. Disentangling contributions of point and line defects in the Raman spectra of graphene-related materials. *2D Mater.* **2017,** *4* (2), 025039.

(76) Puech, P.; Jeanningros, M.; Neumeyer, D.; Monthioux, M. Addressing the effect of stacking faults in X-ray diffractograms of graphite through atom-scale simulations. *Carbon Trends* **2023,** *13*, 100311.

(77) Ros, T. G.; van Dillen, A. J.; Geus, J. W.; Koningsberger, D. C. Surface Oxidation of Carbon Nanofibres. *Chem. - Eur. J.* **2002,** *8* (5), 1151.

(78) Gengenbach, T. R.; Major, G. H.; Linford, M. R.; Easton, C. D. Practical guides for x-ray photoelectron spectroscopy (XPS): Interpreting the carbon 1s spectrum. *J. Vac. Sci. Technol. A* **2021,** *39* (1).

(79) Kovtun, A.; Jones, D.; Dell'Elce, S.; Treossi, E.; Liscio, A.; Palermo, V. Accurate chemical analysis of oxygenated graphene-based materials using X-ray photoelectron spectroscopy. *Carbon* **2019,** *143*, 268.

(80) Morgan, D. J. Comments on the XPS Analysis of Carbon Materials. *C* **2021,** *7* (3), 51.

(81) Estrade-Szwarckopf, H. XPS photoemission in carbonaceous materials: A "defect" peak beside the graphitic asymmetric peak. *Carbon* **2004,** *42* (8), 1713.

(82) Susi, T.; Kaukonen, M.; Havu, P.; Ljungberg, M. P.; Ayala, P.; Kauppinen, E. I. Core level binding energies of functionalized and defective graphene. *Beilstein J. Nanotechnol.* **2014,** *5*, 121.

(83) Davì, R.; Carraro, G.; Stojkovska, M.; Smerieri, M.; Savio, L.; Gallet, J.-J.; Bournel, F.; Rocca, M.; Vattuone, L. Intercalation and reactions of CO under single layer graphene/Ni(111): the role of vacancies. *Phys. Chem. Chem. Phys.* **2022,** *24* (46), 28486.

(84) Barinov, A.; Malcioğlu, O. B.; Fabris, S.; Sun, T.; Gregoratti, L.; Dalmiglio, M.; Kiskinova, M. Initial Stages of Oxidation on Graphitic Surfaces: Photoemission Study and Density Functional Theory Calculations. *The J. Phys. Chem. C* **2009,** *113* (21), 9009.

(85) Kim, J.; Lee, N.; Choi, D.; Kim, D. Y.; Kawai, R.; Yamada, Y. Pentagons and Heptagons on Edges of Graphene Nanoflakes Analyzed by X-ray Photoelectron and Raman Spectroscopy. *J. Phys. Chem. Lett.* **2021,** *12* (40), 9955.

(86) Diana, N.; Yamada, Y.; Gohda, S.; Ono, H.; Kubo, S.; Sato, S. Carbon materials with high pentagon density. *J. Mater. Sci.* **2021,** *56* (4), 2912.

(87) Kundu, S.; Wang, Y.; Xia, W.; Muhler, M. Thermal Stability and Reducibility of Oxygen-Containing Functional Groups on Multiwalled Carbon Nanotube Surfaces: A Quantitative High-Resolution XPS and TPD/TPR Study. *The J. Phys. Chem. C* **2008,** *112* (43), 16869.

(88) Yue, Z. R.; Jiang, W.; Wang, L.; Gardner, S. D.; Pittman, C. U. Surface characterization of electrochemically oxidized carbon fibers. *Carbon* **1999,** *37* (11), 1785.

(89) Smith, M.; Scudiero, L.; Espinal, J.; McEwen, J.-S.; Garcia-Perez, M. Improving the deconvolution and interpretation of XPS spectra from chars by ab initio calculations. *Carbon* **2016,** *110*, 155.

(90) Zhou, J.-H.; Sui, Z.-J.; Zhu, J.; Li, P.; Chen, D.; Dai, Y.-C.; Yuan, W.-K. Characterization of surface oxygen complexes on carbon nanofibers by TPD, XPS and FT-IR. *Carbon* **2007,** *45* (4), 785.

(91) Fairley, N.; Compagnini, G.; Scardaci, V.; Baltrus, J.; Roberts, A.; Barlow, A.; Cumpson, P.; Baltrusaitis, J. Surface analysis insight note: Differentiation methods applicable to noisy data for determination of sp^2- versus sp^3-hybridization of carbon allotropes and AES signal strengths. *Surf. Interface Anal.* **2023,** *55* (3), 165.

(92) Herold, F.; Gläsel, J.; Etzold, B. J. M.; Rønning, M. Can Temperature-Programmed Techniques Provide the Gold Standard for Carbon Surface Characterization? *Chem. Mater.* **2022,** *34* (19), 8490.

(93) Rocha, R. P.; Pereira, M. F. R.; Figueiredo, J. L. Characterisation of the surface chemistry of carbon materials by temperature-programmed desorption: An assessment. *Catal. Today* **2023,** *418*, 114136.

(94) Intan, N. N.; Pfaendtner, J. Composition of Oxygen Functional Groups on Graphite Surfaces. *The J. Phys. Chem. C* **2022,** *126* (26), 10653.

(95) Figueiredo, J. L.; Pereira, M. F. R.; Freitas, M. M. A.; Órfão, J. J. M. Characterization of Active Sites on Carbon Catalysts. *Ind. Eng. Chem. Res.* **2007,** *46* (12), 4110.

(96) Saber, J. M.; Kester, K. B.; Falconer, J. L.; Brown, L. F. A mechanism for sodium oxide catalyzed CO2 gasification of carbon. *J. Catal.* **1988,** *109* (2), 329.

(97) Balomenos, E.; Panias, D.; Paspaliaris, İ. Exergy Analysis of Metal Oxide Carbothemic Reduction under Vacuum – Sustainability prospects. *Int. J. Thermodyn.* **2012,** *15* (3), 141.

(98) Wakabayashi, K.; Yoshii, T.; Nishihara, H. Quantitative study on catalysis of unpaired electrons in carbon edge sites. *Carbon* **2023,** *210*, 118069.

(99) Eckmann, A.; Felten, A.; Mishchenko, A.; Britnell, L.; Krupke, R.; Novoselov, K. S.; Casiraghi, C. Probing the Nature of Defects in Graphene by Raman Spectroscopy. *Nano Lett.* **2012,** *12* (8), 3925.

(100) Bagri, A.; Mattevi, C.; Acik, M.; Chabal, Y. J.; Chhowalla, M.; Shenoy, V. B. Structural evolution during the reduction of chemically derived graphene oxide. *Nat. Chem.* **2010,** *2* (7), 581.

(101) Murakami, K.; Kondo, R.; Fuda, K.; Matsunaga, T. Acidity distribution of carboxyl groups in Loy Yang brown coal: its analysis and the change by heat treatment. *J. Colloid Interface Sci.* **2003,** *260* (1), 176.

(102) Liu, S.; Zhang, Z.; Wang, H. Quantum chemical investigation of the thermal pyrolysis reactions of the carboxylic group in a brown coal model. *J. Mol. Model.* **2012,** *18* (1), 359.

(103) Wang, M.-F.; Zuo, Z.-J.; Ren, R.-P.; Gao, Z.-H.; Huang, W. Theoretical Study on Catalytic Pyrolysis of Benzoic Acid as a Coal-Based Model Compound. *Energy Fuels* **2016,** *30* (4), 2833.

(104) Kato, K.; Osuka, A. Platforms for Stable Carbon-Centered Radicals. *Angew. Chem. Int. Ed.* **2019,** *58* (27), 8978.

(105) Saito, K.; Xu, T.; Ishikita, H. Correlation between C═O Stretching Vibrational Frequency and pKa Shift of Carboxylic Acids. *J. Phys. Chem. B* **2022,** *126* (27), 4999.

(106) Semenenko, B.; Esquinazi, P. D. Diamagnetism of Bulk Graphite Revised. *Magnetochemistry* **2018,** *4* (4), 52.

(107) Nair, R. R.; Sepioni, M.; Tsai, I. L.; Lehtinen, O.; Keinonen, J.; Krasheninnikov, A. V.; Thomson, T.; Geim, A. K.; Grigorieva, I. V. Spin-half paramagnetism in graphene induced by point defects. *Nat. Phys.* **2012,** *8* (3), 199.

(108) Deyo, S.; Hershfield, S. Magnetism in graphene flakes with edge disorder. *Phys. Rev. B* **2021,** *104* (1), 014404.

(109) Odintsov, B. M.; Belford, R. L.; Ceroke, P. J.; Clarkson, R. B. Solid−Liquid Electron Density Transfer in Aqueous Char Suspensions by ^{1}H-Pulsed Dynamic Nuclear Polarization at Low Magnetic Field. *J. Am. Chem. Soc*. **1998**, *120* (5), 1076.

(110) Liu, X.; Gu, J.; Wightman, J.; Dorn, H. C. Elucidation of Oxygen Chemisorption Sites on Activated Carbons by ^{1}H DNP for Insight into Oxygen Reduction Reactions. *ACS Appl. Nano Mat*. **2019**, *2* (12), 7488.

(111) Barzola-Quiquia, J.; Esquinazi, P.; Lindel, M.; Spemann, D.; Muallem, M.; Nessim, G. D. Magnetic order and superconductivity observed in bundles of double-wall carbon nanotubes. *Carbon* **2015,** *88*, 16.

(112) Felner, I. Superconductivity and unusual magnetic behavior in amorphous carbon. *Mater. Res. Express* **2014,** *1* (1), 016001.

(113) Felner, I.; Prilutskiy, E. Unusual Magnetic Properties and Superconductivity in Sulfur-Doped Amorphous Carbon Powder. *J. Supercond. Nov. Magn.* **2012,** *25* (8), 2547.

(114) Felner, I. Superconductivity and Unusual Magnetic Features in Amorphous Carbon and in Other Unrelated Materials. *J. Supercond. Nov. Magn.* **2017,** *30* (1), 55.

(115) Barbon, A. In *Electron Paramagnetic Resonance: Volume 26*; Chechik, V.;Murphy, D. M., Eds.; The Royal Society of Chemistry, 2018; Vol. 26.

(116) Diamantopoulou, A.; Glenis, S.; Zolnierkiwicz, G.; Guskos, N.; Likodimos, V. Magnetism in pristine and chemically reduced graphene oxide. *J. Appl. Phys*. **2017**, *121* (4), 043906.

(117) Stoll, S.; Schweiger, A. EasySpin, a comprehensive software package for spectral simulation and analysis in EPR. *J. Magn. Reson.* **2006,** *178* (1), 42.

(118) Brustolon, M.; Barbon, A. In *EPR of Free Radicals in Solids: Trends in Methods and Applications*; Lund, A.;Shiotani, M., Eds.; Springer US: Boston, MA, 2003, DOI:10.1007/978-1-4757-5166-6_2 10.1007/978-1-4757-5166-6_2.

(119) Zhang, Y.; Wang, J.; Zhou, F.; Liu, J. An effective strategy for hydrogen supply: catalytic acceptorless dehydrogenation of N-heterocycles. *Catal. Sci. Technol.* **2021,** *11* (12), 3990.

(120) Hu, H.; Nie, Y.; Tao, Y.; Huang, W.; Qi, L.; Nie, R. Metal-free carbocatalyst for room temperature acceptorless dehydrogenation of N-heterocycles. *Sci. Adv.* **2022,** *8* (4), eabl9478.

(121) Li, X.; Yuan, Z.; Liu, Y.; Yang, H.; Nie, J.; Wang, G.; Liu, B. Nitrogen-Doped Carbon as a Highly Active Metal-Free Catalyst for the Selective Oxidative Dehydrogenation of N-Heterocycles. *ChemSusChem* **2022,** *15* (15), e202200753.

(122) Shang, S.; Li, Y.; Lv, Y.; Dai, W. Metal- and Additive-Free Aerobic Dehydrogenation of N-Heterocycles and Hydrocarbons by N-Doped Carbon. *Asian J. Org. Chem.* **2022,** *11* (7), e202200126.

(123) Sun, K.; Shan, H.; Ma, R.; Wang, P.; Neumann, H.; Lu, G.-P.; Beller, M. Catalytic oxidative dehydrogenation of N-heterocycles with nitrogen/phosphorus co-doped porous carbon materials. *Chem. Sci.* **2022,** *13* (23), 6865.

(124) Enders, L.; Casadio, D. S.; Aikonen, S.; Lenarda, A.; Wirtanen, T.; Hu, T.; Hietala, S.; Ribeiro, L. S.; Pereira, M. F. R.; Helaja, J. Air oxidized activated carbon catalyst for aerobic oxidative aromatizations of N-heterocycles. *Catal. Sci. Technol.* **2021,** *11* (17), 5962.

(125) Ahmed, M. R.; Anaya, I. O.; Nishina, Y. Investigating the radical properties of oxidized carbon materials under photo-irradiation: behavior of carbon radicals and their application in catalytic reactions. *Chem. Commun*. **2024**, *60* (76), 10544.

(126) He, H.; Li, Z.; Li, K.; Lei, G.; Guan, X.; Zhang, G.; Zhang, F.; Fan, X.; Peng, W.; Li, Y. Bifunctional Graphene-Based Metal-Free Catalysts for Oxidative Coupling of Amines. *ACS Appl. Mater. Interfaces* **2019,** *11* (35), 31844.

(127) Mollar-Cuni, A.; Ventura-Espinosa, D.; Martín, S.; García, H.; Mata, J. A. Reduced Graphene Oxides as Carbocatalysts in Acceptorless Dehydrogenation of N-Heterocycles. *ACS Catal.* **2021,** *11* (23), 14688.

(128) Lian, Z.; Si, C.; Jan, F.; Yang, M.; Li, B. Resolving the Mechanism Complexity of Oxidative Dehydrogenation of Hydrocarbons on Nanocarbon by Microkinetic Modeling. *ACS Catal.* **2020,** *10* (23), 14006.

(129) Sedenho, G. C.; De Porcellinis, D.; Jing, Y.; Kerr, E.; Mejia-Mendoza, L. M.; Vazquez-Mayagoitia, Á.; Aspuru-Guzik, A.; Gordon, R. G.; Crespilho, F. N.; Aziz, M. J. Effect of Molecular Structure of Quinones and Carbon Electrode Surfaces on the Interfacial Electron Transfer Process. *ACS Appl. Energy Mater.* **2020,** *3* (2), 1933.